Ore Geology Reviews 65 (2015) 733–748

Contents lists available at ScienceDirect

Ore Geology Reviews

journal homepage: www.elsevier.com/locate/oregeorev

Electron probe microanalysis and microscopy: Principles and applications in characterization of mineral inclusions in chromite from diamond deposit

Donggao Zhao [a,*], Youxue Zhang [b], Eric J. Essene [b,1]

[a] Department of Geological Sciences, Jackson School of Geosciences, University of Texas at Austin, Austin, TX 78712, USA
[b] Department of Earth and Environmental Sciences, University of Michigan, 2534 C.C. Little Building, Ann Arbor, MI 48109, USA

ARTICLE INFO

Article history:
Received 9 April 2014
Received in revised form 9 September 2014
Accepted 15 September 2014
Available online 28 September 2014

Keywords:
Electron probe microanalysis and microscopy
Mineral inclusions
Chromite
Kimberlite
Diamond deposit

ABSTRACT

Electron probe microanalysis and microscopy is a widely used modern analytical technique primarily for quantifying chemical compositions of solid materials and for mapping or imaging elemental distributions or surface morphology of samples at micrometer or nanometer-scale. This technique uses an electromagnetic lens-focused electron beam, generated from an electron gun, to bombard a sample. When the electron beam interacts with the sample, signals such as secondary electron, backscattered electron and characteristic X-ray are generated from the interaction volume. These signals are then examined by detectors to acquire chemical and imaging information of the sample. A unique part of an electron probe is that it is equipped with multiple WDS spectrometers of X-ray and each spectrometer with multiple diffracting crystals in order to analyze multiple elements simultaneously. An electron probe is capable of analyzing almost all elements (from Be to U) with a spatial resolution at or below micrometer scale and a detection limit down to a few ppm.

Mineral inclusions in chromite from the Wafangdian kimberlite, Liaoning Province, China were used to demonstrate the applications of electron probe microanalysis and microscopy technique in characterizing minerals associated with ore deposits, specifically, in this paper, minerals associated with diamond deposit. Chemical analysis and SE and BSE imaging show that mineral inclusions in chromite include anhydrous silicates, hydrous silicates, carbonates, and sulfides, occurring as discrete or single mineral inclusions or composite multiple mineral inclusions. The chromite–olivine pair poses a serious problem in analysis of Cr in olivine using electron probe. Secondary fluorescence of Cr in chromite by Fe in olivine drastically increases the apparent Cr_2O_3 content of an olivine inclusion in a chromite. From the chemical compositions obtained using electron probe, formation temperatures and pressures of chromite and its mineral inclusions calculated using applicable geothermobarometers are from 46 kbar and 980 °C to 53 kbar and 1130 °C, which are within the stability field of diamond, thus Cr-rich chromite is a useful indication mineral for exploration of kimberlite and diamond deposit. A composite inclusion in chromite composed of silicate and carbonate minerals has a bulk composition of 33.2 wt.% SiO_2, 2.5 wt.% Al_2O_3, 22.0 wt.% MgO, 7.5 wt.% CaO, 2.5 wt.% BaO, 0.8 wt.% K_2O, 25.5 wt.% CO_2, and 0.8 wt.% H_2O, similar to the chemical composition of the Wafangdian kimberlite, suggesting that it is trapped kimberlitic magma.

© 2014 Elsevier B.V. All rights reserved.

1. Introduction

Electron probe microanalyzer (EPMA), also known as electron microprobe analyzer (EMPA), is a specialized SEM with multiple wavelength dispersive spectrometers (WDS). Because of uses of secondary electron (SE) and backscattered electron (BSE) detectors and field emission gun (FEG), an EPMA can also be used to acquire images of the sample analyzed at magnifications up to 100,000×. This analytical technique is capable of determining concentrations of elements from Be to U on the micron scale. The term “electron microscope” was first used by Knoll and Ruska (1932), who made the concept of an electron lens a reality. There are two types of electron microscope, i.e., scanning electron microscope (SEM) and transmission electron microscope (TEM). Both SEM and TEM use electrons and electro-magnet lenses to examine small objects. However, SEM usually detects signals emitted from the surface of a sample, while TEM detects signals that pass through the sample, thus requiring the sample to be thin. Other differences between SEM and TEM include 1) accelerating voltages are commonly up to 30 kV in SEM, much lower than 200 kV, a common accelerating voltage for TEM; and 2) SEM uses a focused electron beam to scan across the

---

* Corresponding author at: Department of Geological Sciences, Jackson School of Geosciences, University of Texas at Austin, 2275 Speedway Stop C9000, Austin, TX 78712, USA.
E-mail address: dzhao@utexas.edu (D. Zhao).

[1] Deceased.

http://dx.doi.org/10.1016/j.oregeorev.2014.09.020
0169-1368/© 2014 Elsevier B.V. All rights reserved.

sample surface line by line while TEM uses a parallel static beam. But most modern TEMs have scanning transmission electron microscopy mode (STEM), which also uses a focused electron beam.

In this article, we first review the principles and instrumentation of EPMA technique that is used primarily for X-ray quantitative analysis of chemical compositions and qualitative mapping of elemental distributions in solid materials (Castaing, 1951; Goldstein et al., 2003, 2011; McGee and Keil, 2001; Potts, 1987; Reed, 1993, 1995, 2005; Smith, 1976). We then discuss the applications of EPMA in characterization of mineral inclusions in chromite associated with the diamond deposits in the Wafangdian kimberlite, Liaoning Province, China (No. 50 and No. 42 diatremes). As an important indicator mineral for exploration of kimberlite and diamond deposits (e.g., Dong, 1994; Huang et al., 1992; Mitchell, 1986), chromite could contain abundant mineral inclusions that are small in size ranging from a few microns to hundreds of microns (Zhao, 1998). The high Cr content of chromite is considered to be an indication of high pressure although in general pressure of chromite formation can only be constrained by certain mineral assemblages. Studies on mineral assemblages inside chromite grains from kimberlite help understand origins of kimberlite, diamond and chromite. Previous studies on mineral inclusions in chromite include samples from layered mafic–ultramafic rocks (McDonald, 1965), ophiolites (Matsukage and Arai, 1998; Peng et al., 1995), Alpine-type ultramafic rocks (Peng, 1987), Alaskan-type complexes (Talkington and Lipin, 1985), as well as kimberlites and lamproites (Logvinova and Sobolev, 1991, 1995; Rovsha, 1962). Logvinova and Sobolev (1991, 1995) reported olivine, clinopyroxene, orthopyroxene, garnet, phlogopite and sulfide inclusions in chromite (>0.5 mm) from Siberian kimberlites and Western Australian lamproites.

2. Principle and instrumentation of EPMA

2.1. Principles of EPMA

The first electron microprobe was developed by Raimond Castaing (1951) when he was a doctoral student at the University of Paris. A topical symposium was held by the Microbeam Analysis Society in 1999 to honor Dr. Castaing (see special issue on EPMA published by Microscopy and Microanalysis in 2001, Volume 7, Number 2). An electron microprobe allows elemental concentrations on the micron scale in materials to be quantified routinely at levels as low as 100 ppm or 0.01 wt.%. Quantification of elemental compositions is achieved by comparing the intensity of a characteristic X-ray from an unknown sample with that from a known standard. Using long count times, high beam currents and multipoint background correction, a detection limit of 10 ppm or lower is achievable for some specific analysis, such as the measurement of Ti in quartz (Donovan et al., 2011; Wark and Watson, 2006). EPMA analysis is generally considered to be non-destructive, although the electron beam can damage beam-sensitive materials, such as feldspars, apatite, and glasses, and cause migration of components in alkali- or volatile-bearing phases.

2.1.1. X-ray generation and interaction volume

Characteristic X-rays are generated by a focused electron beam that bombards and interacts with solid materials. Mosley (1913) discovered that the wavelength of the characteristic X-ray from an element is inversely related to its atomic number Z. The range of electrons and X-rays generated by an electron beam within a sample is called interaction or excitation volume, which depends on the energy of the electron beam and average atomic number of the sample. The shape and size of the interaction volume represent the source from which analytical signals originate.

As beam electrons travel through the sample, collision processes between the beam electrons and atoms in the sample are either elastic or inelastic, depending on whether or not energy change is involved. During inelastic collisions, the beam electrons lose part of their energy. If the lost energy is high enough to overcome the critical ionization energy of an element, it will be able to remove an inner-shell electron from the atom, which leaves an inner-shell vacancy. The excited atom is not stable and a higher-shell electron will fall into the vacancy, resulting in release of a characteristic X-ray photon or an Auger electron.

2.1.2. Wavelength dispersion and focusing of characteristic X-ray

X-ray generated in the interaction volume is detected using WDS spectrometers, a key component that makes an EPMA different from other SEM although some modern SEMs may be equipped with a WDS detector. A WDS detector includes a few diffracting crystals and a gas-flow or sealed proportional counter. The X-ray source in the sample, the surface of a diffracting crystal and the gas proportional counter define an imaginary circle of constant diameter, which is called the Rowland's circle (Fig. 1). Diffracting crystals are used to disperse wavelengths of characteristic X-rays and focus a specific X-ray wavelength onto a gas-flow or sealed proportional counters for measurement. Since only a small portion of the X-ray photons from the sample reach a diffracting crystal, the intensity of the X-ray detected by WDS is generally lower than that detected by an energy dispersive spectrometer (EDS) for a given beam current.

2.1.3. Standards and matrix correction

Well characterized and accepted standards are critical for quantitative EPMA. In quantitative EPMA, the concentration of a given element in an unknown sample is obtained by comparing the intensity of a characteristic X-ray of that element with that from a standard with known chemical composition. The intensities of an X-ray line in both sample and standard must also be corrected for matrix effects, deadtime, background and instrumental drift, overlapping, etc. in order to obtain accurate results. According to the Castaing approximation, the intensity I of a characteristic X-ray is proportional to the mass concentration C of the element measured (Reed, 2005). The measured X-ray intensity of an element in EPMA is affected by the concentrations of all the other elements present in the sample. These matrix effects include mainly influence of atomic number (Z), X-ray absorption (A), and secondary

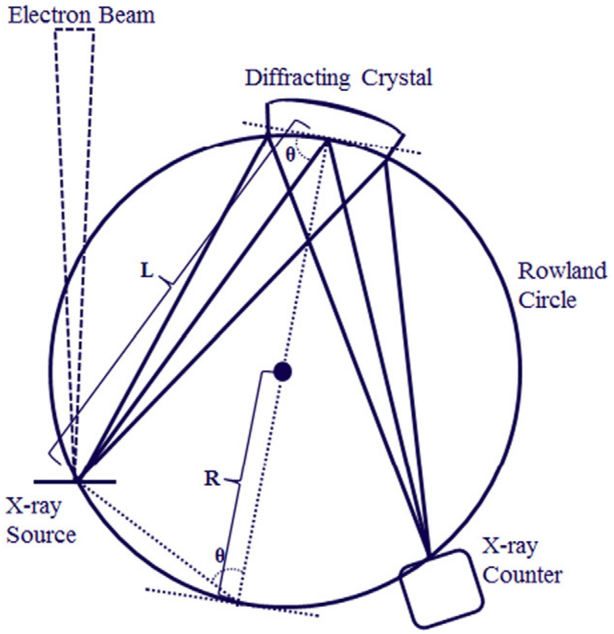

Fig. 1. An imaginary Rowland circle composed of the X-ray source in the sample, the diffracting crystal and the gas proportional counter. R — radius of the Rowland circle, L — detection position which is the distance between the X-ray source and the diffracting crystal, θ — angle of diffraction at which the diffracted characteristic X-rays are in phase and the intensity is constructively enhanced. Since $L = 2R\sin\theta$, combining this equation with Bragg's law, $n\lambda = 2d\sin\theta$, yields $L = n\lambda R / d$.

fluorescence (F). The matrix effects must be corrected in order to obtain the actual concentration of an element.

2.2. Instrumentation of EPMA

Following the trajectories of signals, first the primary electron beam and then the signals from the sample (SE, BSE, X-ray, etc.), the major components of EPMA include 1) electron gun, such as a tungsten filament, LaB6 or field emission gun, used to generate electrons, 2) electron column, composed of a series of electromagnetic lenses, used to manipulate the electron beam in a way similar to light optics, 3) sample chamber with a sample stage adjustable in X, Y, and Z directions, 4) detectors around the sample stage inside the chamber, 5) vacuum system for the column and chamber, 6) WDS spectrometers installed around the electron column, which are used for detecting characteristic X-rays, 7) light microscope for optical observation of the sample, and 8) a control system composed of control interfaces and panel, and computers for data acquisition and processing. The components 1 to 5 above are also common constituents of a typical SEM. A modern EPMA now includes almost all functions of a SEM, equipped with SE, BSE, EDS, and sometimes cathodoluminescence (CL) and/or electron backscattered diffraction (EBSD) detectors (Cherniak et al., 2010).

2.2.1. Electron gun

There are two types of electron guns — thermionic and field emission guns. Most electron microprobes use thermionic tungsten or LaB_6 filaments, but field emission gun electron microprobes are now also available and become popular (MacRae et al., 2006). Thermionic electron emission occurs when the filament material is heated to a temperature of 2600–2700 K so that electrons have a sufficiently high thermal energy to overcome the work function energy of the filament material. A thermionic tungsten filament for an EPMA lasts usually for a few months; and high quality of vacuum within the gun area provided by an ion pump could make a tungsten filament last up to one year. A long lifetime of one or more years is usually achieved by a LaB_6 or FEG gun. In an FEG, electrons are extracted from an extraordinarily sharp tungsten single crystal needle welded to a tungsten hairpin by putting an additional anode of a few kilovolts close to the tip. The main anode is used to accelerate the extracted electrons to the operating voltage. A much high, focused, monochromatic beam current may be obtained from a FEG at a low temperature of 1500 °C.

2.2.2. Electromagnetic lens

Electromagnetic lenses are used to focus and demagnify the electron beam emitted from the gun to an electron probe of approximately 1 to 10 nm on the specimen. An electromagnetic lens is composed of a hollow cylinder made from magnetic material and copper wire coil through which the current is running. All lenses suffer from manufacturing defects or imperfections, so an electron beam may never be brought into perfect focus by an electromagnetic lens. This phenomenon is called spherical aberration. Another type of aberration is chromatic aberration, which is caused by variations in the energy of electrons emitted by the gun.

2.2.3. Probe current and its regulation

The accuracy of quantitative analysis depends partly on the stability of the electron probe current. Probe current must be regularly monitored and corrected during an analytical session. One way to achieve high current stability over long analytical sessions is to use a beam stabilizer or regulating system. Several definitions related to current are used in EPMA: 1) Filament current is the current used to heat the filament for electron emission. 2) Lens current is the current passing through the coil of an electromagnetic lens. An increase in the lens current causes an increase in the strength of the electromagnetic field, which reduces the focal length. 3) Beam current is the total current emitted by the filament. 4) Probe current is the total current delivered to the specimen, which can be measured by using a Faraday cup, i.e., probe current detector (PCD). The probe current represents only a portion of the original beam current from the filament. The probe current is generally maintained at a constant value throughout an analytical session and should be reported in published papers. In the literature, probe current is often referred to as beam current. 5) Specimen current is the residual fraction of the probe current that stays within the sample. Some of the probe current bombarding the sample is backscattered out of the sample (Potts, 1987). For a constant probe current, the specimen current may vary from sample to sample depending on the mean atomic number and conductivity of the sample. Therefore, probe current on Faraday cup, not beam current or specimen current, should be reported in the experimental conditions.

2.2.4. Diffracting crystals

Most electron microprobes are equipped with multiple WDS spectrometers and each spectrometer with multiple diffracting crystals. Use of multiple spectrometers and multiple diffracting crystals are necessary not only for analyzing multiple elements simultaneously, but also for optimizing performance in different wavelength ranges. Common diffracting crystals include lithium fluoride (LiF), pentaerythritol (PET), thallium acid phthalate (TAP), layered diffracting elements (LDE), and pseudocrystals (PC). Theoretically, from Bragg's law, $\sin\theta$ in equation $n\lambda = 2d \sin\theta$ cannot exceed unity; it therefore defines the maximum wavelength that can be diffracted by a diffracting crystal with a given d spacing. Practically the limitations on the wavelength range that can be diffracted by a crystal are also imposed by the design of spectrometer. A lower wavelength limit is imposed by Bragg's equation as it is impossible to move the diffracting crystal too close to the specimen, which limits the θ value. Crystals like LiF with small d spacings (0.4027 nm) are good for X-ray with short wavelengths (e.g., Ti Kα to Br Kα and Sn Lα to U Lα) because their interplanar d spacings are small. Synthetic crystals, such as PET and TAP with larger d spacings, are good for longer wavelengths. For example, PET is generally good for P Kα to Mn Kα, Rb Lα to Ba Lα, and Hf M lines to U M lines; and TAP for F Kα to Si Kα, Rb Lα to Ba Lα, and La M lines to Au M lines. However, the d spacings of PET and TAP are still not large enough to accommodate the long wavelengths. The measurement of long wavelength Kα X-ray lines for light elements such as Be, B, C, N, O and F is better achieved using layered diffracting elements (e.g., LDE1 or LDE2) or pseudocrystals (e.g., PC1, PC2 or PC3). Elements H, He and Li cannot be analyzed by EPMA as their wavelengths are too long. A good diffracting crystal need to be chemically stable and insensitive to room temperature change. An electron probe laboratory is usually kept at a constant temperature close to the temperature of the chilled water to avoid problems with temperature-sensitive crystals. In addition, a diffracting crystal should have good dispersion efficiency, low X-ray absorption, and high reflection efficiency.

2.2.5. X-ray proportional counter

Another major component of a WDS spectrometer is the gas proportional counter (Fig. 1). The gas proportional counter consists of a gas-filled cathode tube with a coaxial thin tungsten wire as anode running through the center of the tube. The potential between the cathode tube and anode wire is at 1000 to 3000 V. There are two types of X-ray proportional counters: 1) gas flow proportional counter for detecting soft or longer wavelength X-ray, and 2) sealed proportional counter for hard or shorter wavelength X-ray as hard X-ray has strong penetrating abilities. When an X-ray photon enters the tube through a thin window, it ionizes atoms of the gas and produces photoelectrons. The photoelectrons are then accelerated toward the anode wire and further ionize other gas atoms producing more electron-ion pairs. This “avalanche” effect produces an amplification of the initial signal, resulting in a charge pulse appearing on the anode. The amplitude or height of the pulse depends on the number of ionizations, which is related to the energy of X-ray photons and gas pressure. For a gas flow proportional counter, a cylinder of P10 gas with 90% Ar and 10% methane is used to provide gas flow to the detector. Therefore, the P10 gas pressure must be constant in order to have reproducibility in counting rates between the standards and the unknowns. In a gas flow proportional counter, approximately 28 eV is needed to create one electron-ion pair for Ar atom. For the Mn Kα, which has an energy of 5.895 keV, about 210 electron-ion pairs will be directly created by the absorption of a single Mn Kα photon. Electron multiplication in the counter depends on the anode voltage. At certain ranges of anode voltages in the counter, the pulse height is directly proportional to the energy of the incident X-ray. The voltage distribution of pulses for a pre-selected time period can be obtained using a single-channel analyzer (SCA), which is used to select and transmit pulses within a predetermined voltage range for further processing. The SCA also serves as an output driver, causing the selected pulses become rectangular pulses of a fixed voltage and time duration.

2.3. Recent advances in EPMA

Recent advances in EPMA includes 1) effects of secondary fluorescence (Cherniak et al., 2010; Llovet and Galan, 2003; Llovet et al., 2012; Maaskant and Kaper, 1991; Myklebust and Newbury, 1994), 2) characterization and evaluation of standard or reference materials (Carpenter, 2008; Carpenter and Vicenzi, 2012; Zhao, 2012), 3) use of FEG-EPMA, L line X-ray and low accelerating voltage and improvement of spatial resolution (Armstrong et al., 2013; Hombourger and Outrequin, 2013; McSwiggen et al., 2012), 4) trace element analysis and background fitting (Donovan and Tingle, 1996; Donovan et al., 2011; Williams et al., 1999), 5) EPMA geochronology (Jercinovic and Williams, 2005; Montel et al., 1996; Williams et al., 1999), and 6) and matrix correction procedures (Armstrong, 1995; Pouchou and Pichoir, 1991). Readers may refer to Keil (1967), McGee and Keil (2001) and Conty (2001) among others for early reviews of EPMA applications. An example of secondary fluorescence is discussed in Section 5.2. Other topics are briefly reviewed below.

2.3.1. Characterization and evaluation of standard or reference materials

Availability of adequate amount of stable, well-characterized, homogeneous, inclusion-free standards is the foundation of quantitative EPMA (Castaing, 1951; Potts, 1987; Reed, 2005). Calibration of primary standards and verification of secondary standard allow accurate electron probe microanalysis. The characterization and analysis of minerals as standards or reference materials in EPMA have been discussed and described by Smith (1976), Jarosewich et al. (1980), Jarosewich and MacIntire (1983), Jarosewich and White (1987), Jarosewich et al. (1987), Jarosewich and Boatner (1991), McGuire et al. (1992), Essene and Henderson (1999), and Jarosewich (2002). The EPMA community has benefited greatly from these invaluable mineral standards. However, recent studies show that most accepted mineral standards are not well-characterized, homogeneous, or inclusion-free standards (Carpenter, 2008; Carpenter and Vicenzi, 2012; Zhao, 2012). For example, the Kakanui hornblende is a widely used, important primary or secondary EPMA standard for routine analysis of minerals, but BSE imaging reveals that Kakanui hornblende contains micron or submicron inclusions (Carpenter and Vicenzi, 2012) and X-ray quantitative analysis confirms that the micron or sub-micron scale inclusions exist in the Kakanui hornblende (Zhao, 2012). Therefore, the Kakanui hornblende may not be a suitable standard, especially for elements such as Na, Ca, Mg and Fe. EPMA technique is still deficient with respect to well-characterized standards. Development and characterization of EPMA standards certainly deserve more attentions from the international microanalysis community. There is an attempt currently in China to establish a nationwide database for certified microanalysis standards (Jianxiong Zhou, personal communication).

2.3.2. FEG-EPMA, L line X-ray, and improvement of spatial resolution

The use of the Schottky thermal FEG in EPMA makes a stable, bright and small electron beam available for WDS quantitative analysis. As a result, FEG-EPMA dramatically improved the spatial resolution of microanalysis to submicron scale by using low accelerating voltage and L line X-ray (Armstrong et al., 2013; Hombourger and Outrequin, 2013; McSwiggen, 2014; McSwiggen et al., 2012, 2014). Armstrong et al. (2013) demonstrated that an FEG-EPMA, operated at a low accelerating voltage (e.g. 7 keV), is capable of X-ray imaging down to 200 nm spatial resolution and accurate quantitative analyses for an area as small as 300–100 nm without contributions from surrounding material for individual grains. This improvement of EPMA performance provides exciting new capabilities in analyses of geological and material samples down to the nano-scale. In addition, high-resolution imaging available with an FEG-EPMA also improves the quality of microanalyses. For example, in analysis of sub-micron crystallites in a volcanic glass, high spatial resolution imaging will assist in identifying areas where the crystallites exist and determining what to analyze. If the volcanic glass matrix is analyzed, high spatial resolution imaging can help to avoid the crystallites to be detected (McSwiggen et al., 2012, 2014).

With low accelerating voltage, only X-ray lines of low energy are excited. They include K lines for atomic numbers less than 22 and L and M lines for atomic numbers greater than 22. Advantages of low accelerating voltage (approximately < 5 kV) include improved analytical spatial resolution, reduction of secondary fluorescence effect, and decrease of charging effect. However, it can become a challenge because X-ray lines of low energy are subject to peak shift, peak overlap, absorption of soft X-ray in high-Z elements making calculation of composition difficult, and low fluorescence yields of L and M lines compared to the K lines. The latter problem is often responsible for low intensities of certain lines (Hombourger and Outrequin, 2013). A major strength of a stable and high beam current FEG-EPMA is its ability to accurately quantify elements down to a few ppm.

2.3.3. Trace element analysis and background fitting

The EPMA technique is routinely used for quantification of major elements and trace elements with concentration greater than 0.01 wt.% or 100 pm. However, trace element measurements below 100 ppm using EPMA are challenging as the measurements are limited by both the precision of the background measurement and the accuracy with which background levels are determined. Donovan et al. (2011) recently developed a procedure using multi-point background fitting to better fit the shape of the background of a trace element peak, which significantly improved the peak/background ratio, accuracy and detection limits for many trace elements such as titanium in quartz (Wark and Watson, 2006). Combining with quantitative blank correction routine and aggregated counting method using multiple spectrometers, the use of multi-point background fitting improved detection limits down to a few ppm for Ti and Al measurement in quartz (Donovan et al., 2011).

2.3.4. EPMA geochronology

A recent application of EPMA is for geochronology investigations by measuring trace amount U, Th, and Pb in accessory minerals such as monazite, xenotime, and thorite. It is assumed that the initial isotopic ratios for these elements were typical for the earth's crust, so the EPMA-measured chemical concentrations may serve as a proxy for the actual isotopic abundances. Radiometric ages are then calculated in the conventional manner using these proxy isotopic data, and are subject to the usual considerations such as closure of the mineral system and the accumulation of measurable daughter Pb (Jercinovic and Williams, 2005; Montel et al., 1996; Williams et al., 1999). As high beam current and lengthy counting times are employed by EPMA for characterization of accessory minerals for geochronology, it requires consideration of beam damage effects and detailed assessment of background shapes, intensities and interferences. The spectra relevant to measurement of Y, Th, Pb, and U are complex, especially in REEbearing minerals. Acquisition of detailed wave scans allows recognition of background and peak interferences, as well as curvature. Background intensities can be fitted from scan data using multi-point background method (Donovan et al., 2011). X-ray mapping allows delineation of domains, guiding background acquisition and detailed quantitative analysis. An FEG-EPMA provides optimized parameters such as beam conditions and spatial resolution and thus further improves the accuracy and precision of U, Th and Pb measurement for geochronology (Hombourger and Outrequin, 2013).

2.3.5. Matrix correction procedures

There are several matrix correction methods, such as calibration curves (Ziebold and Ogilvie, 1964), Bence–Albee (e.g., Armstrong, 1988; Bence and Albee, 1968), ZAF (e.g., Armstrong, 1995) and PAP (e.g., Armstrong, 1995; Brown, 1991; Packwood, 1991; Pouchou and Pichoir, 1991). Over the past years much work has been done to develop and refine these programs for correcting raw intensity data for the effects of atomic number Z, absorption A and fluorescence F of X-rays. In the ZAF correction, the measured X-ray intensity is multiplied by a number of factors that model the influences of the effects listed. However, the ZAF correction does not account for depth distribution of X-rays and is not very reliable for light elements, i.e., elements with X-ray energies less than 1 keV. A modified ZAF correction procedure called the PAP method was developed to better account for the depth distribution of X-rays produced from a sample (Pouchou and Pichoir, 1986a,b, 1988, 1991). To further optimize quantitative analyses for elements with low X-ray energies, it is best to use a standard of similar composition to minimize matrix effects, for example, use a fluorapatite standard rather than a fluorphlogopite or fluorite standard to analyze F in apatite. The matrix correction programs are now integrated with real-time data collection and corrections. Armstrong (1991, 1995) developed programs that allow correction of electron microprobe intensity measurements by selecting from a list of available algorithms for the effects of atomic number, absorption, and fluorescence.

3. Sample preparation, samples studied, and analytical procedures

3.1. Sample preparation

The surface of a sample for EPMA must be flat and unscratched for quantitative analysis as geometry of sample to detector is critical and well-polished samples minimize the effects caused by uneven sample surfaces that result in uneven production of X-rays from the sample, erroneous absorption correction and spurious results. In order to avoid poor vacuum, contamination of the electron column, and damage to the detectors inside the sample chamber, small mineral grains or porous or outgassing samples must be first vacuum impregnated using epoxy before polishing. If a sample is not conductive, carbon coating is necessary as carbon is conductive and almost transparent to the X-ray from a sample. Practically, when a polished sample is carbon coated, a piece of flat golden brass can be coated together with the sample to estimate the thickness of carbon coating. When the surface of the brass turns to be blue, carbon coating is about 25 nm thick (Kerrick et al., 1973).

3.2. Samples studied

The chromite samples studied were recovered from the No. 50 and No. 42 kimberlite diatremes of the Wafangdian Diamond Deposit, Liaoning Province, China. In the North China Craton, hundreds of kimberlite diatremes and dikes have been located (Dong, 1994; Huang et al., 1992). The kimberlite cluster in Wafangdian, Liaoning Province is at the south end of the East Liaoning Uplift of the North China Craton and has more than 100 kimberlite bodies. They are located about 30–40 km east of the Tanlu Fault, a major NNE-trending transcurrent structure in East China extending thousands of kilometers from Northeast China to Central China. The Wafangdian kimberlite was thought to have been emplaced about 400 to 500 Ma ago (Huang et al., 1992). Although alteration of the kimberlite such as serpentinization and carbonatization is extensive, phenocryst or xenocryst minerals such as anhedral olivine, phlogopite, pyrope, chromite, diamond and zircon are common.

3.3. Analytical procedures

Chromite grains were first examined under optical microscope for shape, size and possible fracture penetrating into the inside of chromite crystals before polishing. Mineral inclusions in chromite were then exposed by polishing. Most chromite hosts and their mineral inclusions were analyzed using EPMA with a focused beam in spot mode at the University of Michigan. However, carbonates and hydrous silicate phases were analyzed using a raster mode of 3 × 3 μm. Peak and background counting times were set at 30 and 15 s except for Si in chromite that was counted for 120 s to increase precision. To examine homogeneity, multiple points were analyzed for each phase.

3.3.1. Procedure for chromite host

For chromite or spinel analyses, synthetic ferrosilite was used as standard for Si, synthetic geikielite for Mg and Ti, chromite for Al, synthetic V_2O_5 for V, synthetic Cr_2O_3 for Cr, Broken Hill rhodonite for Mn, hematite (Elba) for Fe, and synthetic NiS for Ni. Chromite was analyzed at an accelerating voltage of 10 kV and a beam current of 10 nA. The lower voltage was used to reduce the potential fluorescence effect of Cr by Fe. Chromite from kimberlite may have a significant Si content. To increase the precision and accuracy of Si measurements, the counting time for Si in chromite was intentionally set at 120 s.

3.3.2. Procedure for anhydrous silicate minerals

For analysis of silicate minerals (olivine, pyroxene, and garnet), an accelerating voltage of 15 or 10 kV and a beam current of 10 nA were used. For analysis of Cr in olivine inclusions in chromite, a different accelerating voltage of 30 kV was used to investigate fluorescent effect of Cr in chromite host by Fe in olivine inclusions. The standards used are clinopyroxene (from Irving) as a standard for Si and Ca, olivine for Mg, ferrosilite for Fe, almandine (from Ingamells) for Al, uvarovite for Cr, geikielite for Ti, rhodonite for Mn, NiS for Ni, and jadeite (from ANU) for Na.

3.3.3. Procedure for hydrous silicate minerals

The standards for analysis of phlogopite are clinopyroxene (Irving) for Si and Ca, andalusite for Al, synthetic geikielite for Ti, synthetic uvarovite for Cr, Kakanui hornblende for Mg and Na, K-feldspar for K, synthetic ferrosilite for Fe, Broken Hill rhodonite for Mn, synthetic NiS for Ni, fluortopaz (Topaz Mountain) for F, and synthetic Ba–Cl apatite for Cl and Ba.

3.3.4. Procedure for carbonate minerals

The standards for analysis of carbonate phases are calcite for Ca, dolomite for Mg, rhodochrosite for Mn, siderite for Fe, celestite for Sr, and sanbornite for Ba. The CO_2 is calculated by stoichiometry.

3.3.5. Procedure for sulfides

For sulfide, synthetic FeS was used as standard for S and Fe, Scott chalcopyrite for Cu, synthetic NiS for Ni, synthetic ZnS for Zn, synthetic MnS for Mn and synthetic CoS for Co. Sulfide was analyzed at an accelerating voltage of 20 kV and a beam current of 10 nA or at 10 kV and 20 nA if K and Cr were included. The lower voltage was also used to reduce the fluorescence effect of Fe by Ni.

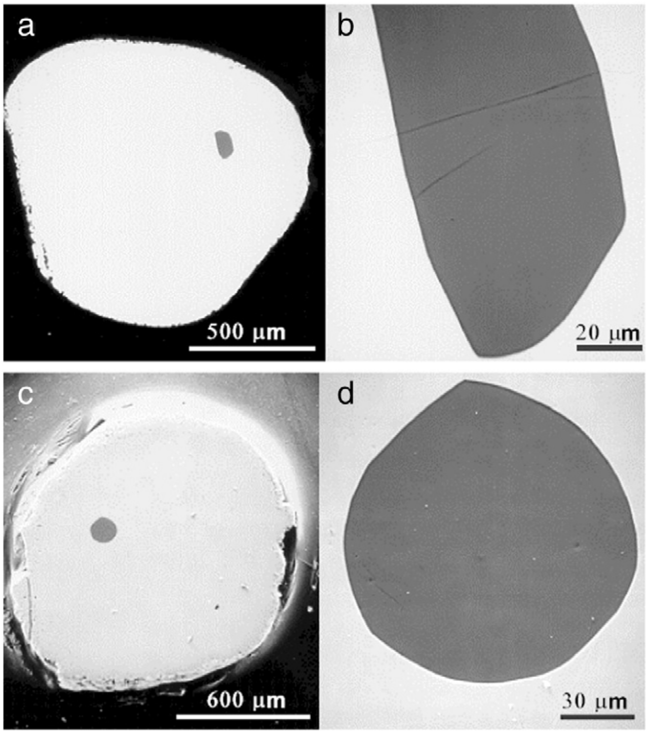

Fig. 2. BSE images of rounded, anhedral chromite and its mineral inclusions: a) chromite host LN42SP14 and b) a euhedral, elongated olivine inclusion; c) chromite host LN50SP04 and d) a subhedral olivine inclusion.

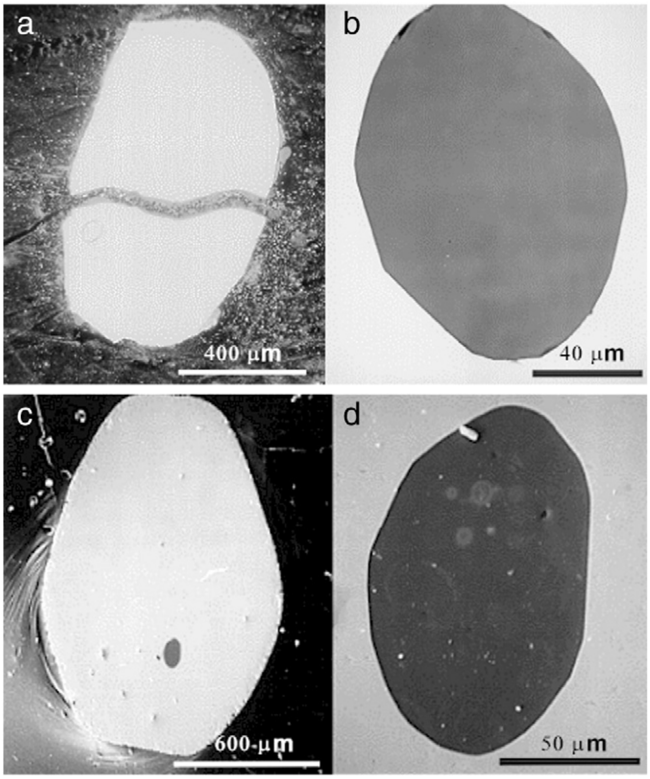

Fig. 3. BSE images of subhedral chromite and its mineral inclusions: a) chromite host LN42SP16 and b) a subhedral olivine inclusion; c) chromite host LN50SP03 and d) a subhedral olivine inclusion.

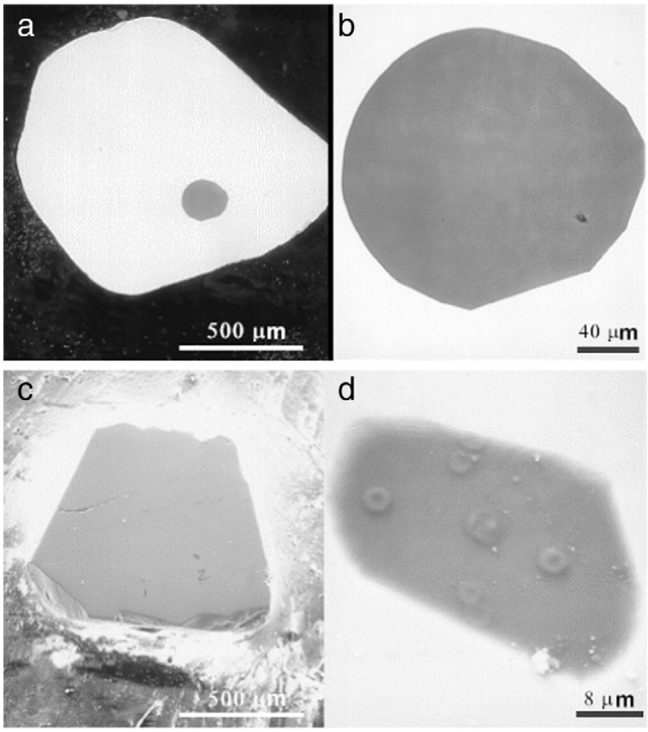

Fig. 4. BSE images of euhedral chromite and its mineral inclusions: a) chromite host LN50SP06 and b) subhedral olivine inclusion; c) chromite host LN42SP2 with two small olivine inclusions and d) one euhedral olivine inclusion.

4. Imaging and analytical results of chromite and its mineral inclusions

Chromite from the Wafangdian kimberlite occurs as xenocrysts, groundmass phenocrysts, mineral inclusions in diamond, and reaction products of other minerals (Dong, 1994; Huang et al., 1992; Mitchell, 1986). The host chromites are anhedral to rounded (Fig. 2), subhedral (Fig. 3), or euhedral (Fig. 4) in shape and ranges in diameter from 0.1 to 2 mm, with some up to 5 mm. Unlike mineral inclusions in diamond, mineral inclusions inside a chromite host cannot be seen before polishing due to its opacity. Chromite crystals were constantly examined using optical microscope during polishing process to check for the exposure of inclusions. Then the inclusion-bearing chromites were examined with BSE and SE imaging techniques. Approximately 10% of the chromite grains polished contain mineral inclusions. Mostly, only one inclusion was exposed in a chromite crystal (Figs. 2–4). Occasionally more than one mineral inclusion can be found within a chromite crystal on a polished surface (Figs. 4c, 5). Composite inclusions are rare but were also discovered (Fig. 6). For example, in a chromite grain (LN50SP07), one composite inclusion assemblage consists of phlogopite, magnesite, dolomite, norsethite [$MgBa(CO_3)_2$], and a pure SiO_2 phase (Fig. 6a).

Olivine is the most abundant mineral inclusion in chromite. The olivine inclusions occur as isolated anhedral or spherical (Figs. 2c, 5b), subhedral (Figs. 2d, 3b, d, 4b), and euhedral or elongated (Figs. 2b, 4d) crystals in chromite hosts. The diameter of the olivine inclusions varies from a few μm to up to 150 μm, but most are less than 100 μm. One garnet and two olivine inclusions were identified in a 2-mm long chromite grain (Fig. 5a). The garnet inclusion is about 180 μm in size and possesses a secondary symplectitic rim composed of a complex intergrowth of fine-grained aluminous orthopyroxene, clinopyroxene and spinel (Fig. 5d). Symplectitic pyroxene and spinel are very small in size, approximately 5 to 10 μm (Fig. 5e, f). Phlogopite and carbonate phases coexist in composite inclusions (Fig. 6). Carbonate minerals also occur as single isolated inclusions (Fig. 7c). Carbonate inclusions are

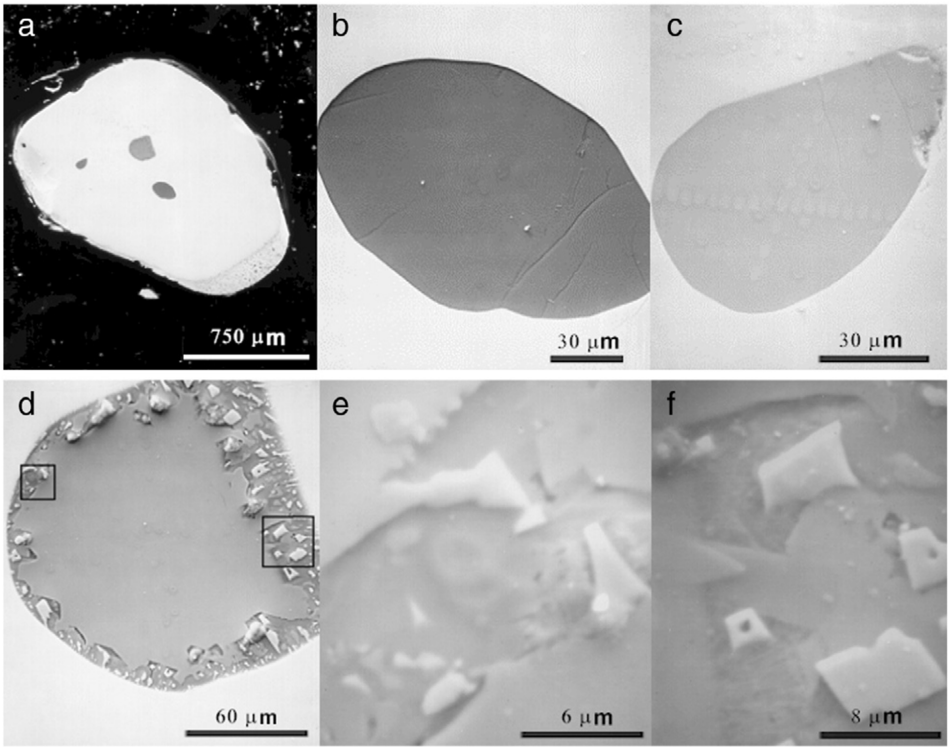

Fig. 5. BSE images of chromite LN42SP01 and its mineral inclusions: a) chromite host and three inclusions; b) and c) smaller anhedral olivine inclusions in the chromite host; d) subhedral pyrope inclusion with a symplectitic rim of aluminous spinel and pyroxenes in the chromite host; e) and f) enlarged images of the two inset squares in image d.

common in chromite. The species identified include Ca carbonate (calcite or aragonite), magnesite, dolomite, and norsethite. A sulfide inclusion was identified in chromite LN50SP10 (Fig. 7d). The sulfide inclusion is about 35 μm in diameter. In addition, a silicate similar to talc in composition was found in a chromite (LN50SP01).

The chemical compositions of chromite and its mineral inclusions acquired using EPMA are given in Tables 2–7. Ferric iron in chromite/spinel and garnet was calculated on the basis of charge balance and stoichiometry. Total iron was treated as Fe^{2+} and was not calculated as ferric and ferrous iron for olivine, orthopyroxene and clinopyroxene in the tables.

4.1. Chromite host

The chemical compositions of the kimberlitic chromite from the No. 50 and No. 42 diatremes of the Wafangdian kimberlite are given in Table 1. The Mg # of the chromite is 100Mg / (Mg + Fe^{2+}) by atom and it varies from 47 to 67 (Fig. 5a). The Cr_2O_3 content of the chromite ranges from 42 to 66 wt.% (Fig. 5b). The SiO_2 content of the chromite is approximately 0.10 wt.% (Fig. 8c). The TiO_2 content of the chromite varies from 0 to 3.78 wt.%, but most are below 0.5 wt.% (Table 1).

4.2. Anhydrous silicates

4.2.1. Olivine

Olivine inclusions in chromite have a Mg # (=100Mg / (Mg + Fe) by atom) of 88 to 93, with a peak between 92 and 93 (Table 2; Fig. 9a). The NiO contents vary over a range from 0.22 to 0.44 wt.%, but most are around 0.40 wt.% (Table 2; Fig. 9b). The CaO contents of the olivine inclusions in chromite are very low and do not exceed 0.06 wt.% (Table 2; Fig. 10), similar to those for the olivine inclusions in diamond from the same location (Zhao, 1998). The analyses after removing the chromite host shows that the Cr_2O_3 contents of one olivine inclusion are from 0.06 to 0.16 wt.% (LN42SP11).

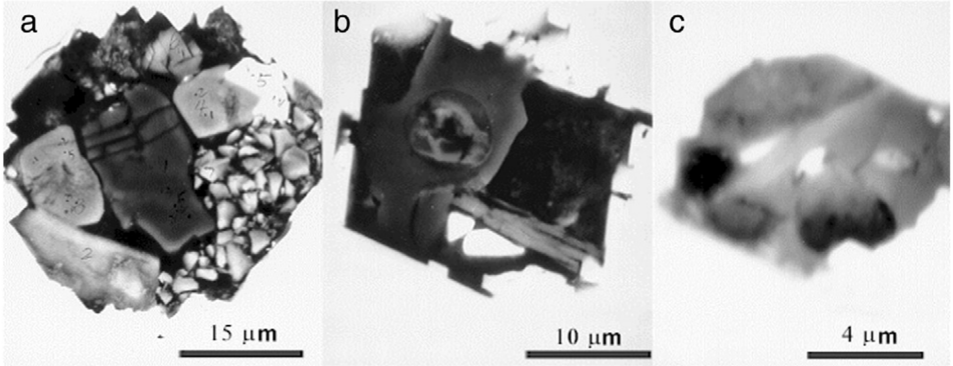

Fig. 6. BSE images of composite mineral inclusions in chromite: a) a composite inclusion composed of magnesite, dolomite, norsethite, phlogopite and a SiO_2 phase in chromite LN50SP07; b) a composite inclusion composed of dolomite, norsethite and phlogopite in chromite LN42SP06; and c) a composite inclusion composed of norsethite and phlogopite in chromite LN42SP07.

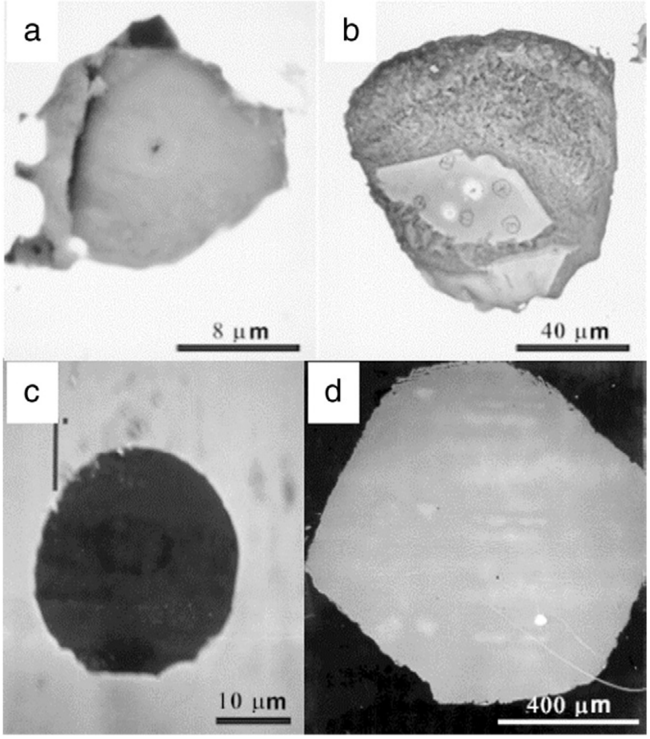

Fig. 7. BSE image of discrete mineral inclusions in chromites: a) phlogopite inclusion in chromite LN42SP07; b) Ca-carbonate inclusion in chromite LN42SP07; (c) rounded magnesite inclusion in chromite LN50SP05; and (d) chromite host LN50SP10 and a sulfide inclusion (bright spot in the lower right area).

4.2.2. Pyrope and its symplectitic pyroxenes

The garnet inclusion with a secondary symplectitic rim in chromite sample LN42SP01 is a homogeneous subcalcic Cr-pyrope (Fig. 5). The Cr_2O_3, Al_2O_3 and TiO_2 contents of the garnet are comparable to those for garnet inclusions in diamond (Zhao, 1998), but the CaO content is higher than those for garnet inclusions in diamond (Table 3). On a CaO versus Cr_2O_3 diagram, this garnet plots in the lherzolitic field. There is no excess Si in the garnet; and the garnet does not contain exsolution lamellae of pyroxenes, implying that it did not equilibrate above 60–80 kbar. The pyroxenes identified in the symplectitic rim include aluminous enstatite and diopside (Table 3). The chromite host of the garnet inclusion is enriched in Cr_2O_3 (63.31 wt.%; Table 1).

4.3. Hydrous silicates

4.3.1. Phlogopite

Four phlogopite inclusions were identified in chromite. The phlogopite inclusions coexist with carbonate minerals, such as magnesite, dolomite and norsethite (Fig. 6) or occur as isolated inclusions (Fig. 7a). The phlogopite inclusions contain low TiO_2 (<0.8 wt.%), high Cr_2O_3 (>2.0 wt.%) and MgO (>22.5 wt.%) (Table 4), similar to phlogopites in the mantle xenoliths from kimberlite (Zhao, 1998). The low TiO_2 and high Cr_2O_3 and MgO contents are characteristics of the high-Cr phlogopites in kimberlite from the same diatreme (Huang et al., 1992), which are considered to have compositions equivalent to those of primary phlogopites in lherzolites and therefore possibly to be derived from such a source (Mitchell, 1986). The similarity of the phlogopite inclusions in chromite to those in mantle xenoliths and in kimberlite suggests that they are primary mantle phlogopites. In addition, the phlogopite inclusions have low K_2O contents of less than 5.5 wt.%, implying that they are chloritized or submicroscopically intergrown with other sheet silicates (Table 4).

4.3.2. Talc

A magnesium silicate phase with a low analytical total was found in chromite LN50SP01 (Table 5) and is tentatively identified as talc. The rim of this inclusion contains magnetite. Talc is stable at low temperatures and high pressures (Hoschek, 1995), and the relatively high iron concentration is consistent with low-temperature formation (Forbes, 1971). The low totals after adding H_2O using talc formula may indicate either difficulty in EPMA or the phase is kelorite, a subgroup of talc (Brindley et al., 1977). This phase likely formed during mantle metasomatism at relatively low temperatures.

4.4. Carbonates

4.4.1. Ca carbonate

Two single Ca carbonate inclusions were identified in samples LN42SP06 and LN42SP07, respectively (Fig. 7b). The Ca carbonate shows very limited compositional variation and contains as high as 98.6% $CaCO_3$ and only 0.8% $MgCO_3$, 0.3% $MnCO_3$, and 0.4% $FeCO_3$ (Table 6).

4.4.2. Magnesite

Magnesite was found in chromite hosts LN50SP05 and LN50SP07. In sample LN50SP05, magnesite occurs as an isolated inclusion (Fig. 7c); in sample LN50SP07, magnesite coexists with dolomite, norsethite and phlogopite (Fig. 6a). The isolated magnesite (LN50SP05) contains 93.5% $MgCO_3$, 4.5 mol% $FeCO_3$ and 2.0 mol% $CaCO_3$, whereas, the magnesite in the multimineralic inclusion (LN50SP07) is 99% $MgCO_3$ (Table 6).

4.4.3. Dolomite

Dolomite was found in chromite hosts LN42SP06 and LN50SP07. Dolomite coexists with magnesite, norsethite and phlogopite in sample LN50SP07 (Fig. 6a); and coexists with Ca-carbonate and norsethite in sample LN42SP06 (Fig. 6b). In both cases, dolomite coexists with norsethite (see below) in the composite inclusions. A similar and Ba-rich association, i.e., dolomite with exsolved Ca–Ba carbonate, was reported in the Benfontein calcite kimberlite, South Africa (Mitchell, 1994). The dolomite in LN42SP06 contains up to ~2.2 mol% $FeCO_3$ (Table 6), also similar to that found in the groundmass of the Benfontein calcite kimberlite (Mitchell, 1994).

4.4.4. Norsethite

Norsethite, $BaMg(CO_3)_2$, was found in both the No. 50 and the No. 42 diatremes, although only a half dozen norsethite occurrences are known (Böttcher et al., 1997; Mrose et al., 1961; Steyn and Watson, 1967; Sundius and Blix, 1965). The chemical composition of norsethite from both diatremes is similar (Table 6). Norsethite from the No. 50 diatreme (LN50SP07) coexists with magnesite, dolomite and phlogopite (Fig. 6a) and contains minor amounts of $FeCO_3$ and $CaCO_3$ components (Table 6). Norsethite from the No. 42 diatreme (LN42SP06) coexists with dolomite and phlogopite (Fig. 6b) and contains minor amount of $FeCO_3$ component (Table 6).

4.5. Sulfides

In a euhedral chromite crystal (LN50SP10), a sulfide grain of 30 μm diameter was identified. This sulfide inclusion is an irregular six-sided polygon in shape (Fig. 7d) and heterogeneous in composition (Table 7). The Fe, Ni and Cu contents vary significantly, with Fe from 34 to 57 wt.%, Ni from <1 to 24 wt.%, and Cu from <1 to 6 wt.%. The Σcation/sulfur ratios of analyses are less than unity. Some analyses (e.g., points 11 and 15 in Table 7) have Σcations slightly higher than 3 when sulfur is normalized to 4 atoms per formula unit, similar to R_3S_4 minerals in the linnaeite group (violarite — $FeNi_2S_4$, daubreelite — $FeCr_2S_4$, greigite — Fe_3S_4 and carrollite — $CuCo_2S_4$). In terms of bulk chemical compositions, the sulfide in the chromite LN50SP10 is similar to those found in the diamond from the same location (Zhao, 1998).

Table 1

Compositions of chromites from the Wafangdian kimberlite diatremes, Liaoning Province, China. Mg # = 100Mg / (Fe^{2+} + Mg); Cr # = 100Cr / (Cr + Alvi), both by atoms.

Sample	LN42SP01	LN42SP02	LN42SP03	LN42SP04	LN42SP13	LN42SP14	LN42SP16	LN50SP02	LN50SP04	LN50SP05	LN50SP06	LN50SP07	LN50SP08	LN50SP09	LN50SP10	LN50SP11	LN50SP12	LN50SP13	LN50SP14
SiO_2	0.07	0.04	0.10	0.10	0.18	0.16	0.07	0.12	0.15	0.09	0.09	0.10	0.03	0.11	0.06	0.08	0.08	0.04	0.10
TiO_2	0.12	0.03	0.27	1.51	0.04	0.08	0.33	0.06	0.40	0.39	1.22	2.96	0.11	0.44	0.43	0.08	0.13	0.06	3.78
Al_2O_3	6.61	7.45	8.84	5.62	5.67	5.50	4.90	5.84	18.61	5.32	5.21	5.43	8.74	13.82	22.93	6.31	5.92	11.09	4.65
Cr_2O_3	63.31	63.44	51.85	57.16	65.47	65.14	60.45	64.73	44.77	64.04	60.03	55.44	61.35	46.31	42.08	63.98	64.27	59.89	53.65
V_2O_3	0.23	0.24	0.27	na	0.14	0.24	0.20	0.26	0.15	0.26	0.27	0.39	0.29	0.21	0.21	0.24	0.24	0.25	0.42
TFeO	16.97	16.91	26.55	23.77	14.90	16.20	23.57	15.53	21.10	17.20	20.74	23.67	18.09	27.01	21.23	16.57	16.54	15.56	25.01
NiO	0.10	0.07	0.11	0.11	0.10	0.10	0.11	0.01	0.19	0.11	0.13	0.15	0.10	0.17	0.16	0.04	0.12	0.08	0.18
MnO	0.09	0.14	0.37	0.00	0.22	0.30	0.37	0.04	0.25	0.31	0.35	0.33	0.31	0.34	0.32	0.29	0.30	0.24	0.34
MgO	11.46	11.63	9.66	10.47	13.84	12.62	9.27	12.40	13.86	12.52	11.18	10.77	11.29	11.28	12.89	12.22	12.72	13.03	11.09
ZnO	0.11	0.11	0.05	na	0.04	0.06	0.11	0.07	0.06	0.05	0.09	0.07	0.11	0.07	0.10	0.02	0.05	0.08	0.07
Σ	99.08	100.08	98.07	98.75	100.59	100.40	99.37	99.06	99.51	100.29	99.30	99.30	100.43	99.77	100.41	99.84	100.37	100.32	99.27
Fe_2O_3	1.93	1.81	9.40	6.38	3.26	2.85	5.77	1.87	8.07	3.66	4.90	5.65	2.33	11.05	5.71	2.64	3.39	2.03	7.03
FeO	15.24	15.29	18.10	18.03	11.96	13.64	18.38	13.85	13.84	13.91	16.33	18.59	16.00	17.07	16.09	14.19	13.50	13.74	18.69
Σ	99.27	100.26	99.01	99.39	100.92	100.69	99.95	99.24	100.32	100.66	99.79	99.87	100.66	100.87	100.98	100.10	100.71	100.52	99.98
Si	0.002	0.001	0.003	0.003	0.006	0.005	0.002	0.004	0.005	0.003	0.003	0.003	0.001	0.004	0.002	0.003	0.003	0.001	0.003
Alvi	0.261	0.290	0.351	0.224	0.218	0.213	0.197	0.229	0.681	0.207	0.206	0.215	0.338	0.523	0.825	0.246	0.229	0.419	0.185
Fe^{+3}	0.049	0.045	0.238	0.163	0.080	0.071	0.148	0.047	0.189	0.091	0.124	0.143	0.057	0.267	0.131	0.066	0.084	0.049	0.178
Ti	0.003	0.001	0.007	0.039	0.001	0.002	0.008	0.001	0.009	0.010	0.031	0.075	0.003	0.011	0.010	0.002	0.003	0.002	0.096
Cr	1.674	1.655	1.382	1.530	1.685	1.695	1.628	1.706	1.099	1.670	1.594	1.475	1.590	1.176	1.016	1.673	1.669	1.520	1.428
V	0.006	0.006	0.007	0.000	0.004	0.006	0.005	0.007	0.004	0.007	0.007	0.010	0.008	0.005	0.005	0.006	0.006	0.006	0.011
Fe^{+2}	0.426	0.422	0.510	0.510	0.326	0.375	0.524	0.386	0.359	0.384	0.459	0.523	0.438	0.459	0.411	0.393	0.371	0.369	0.526
Ni	0.003	0.002	0.003	0.003	0.003	0.003	0.003	0.000	0.005	0.003	0.003	0.004	0.003	0.004	0.004	0.001	0.003	0.002	0.005
Mn	0.003	0.004	0.011	0.000	0.006	0.008	0.011	0.001	0.007	0.009	0.010	0.009	0.009	0.009	0.008	0.008	0.008	0.007	0.010
Mg	0.572	0.572	0.485	0.528	0.672	0.619	0.471	0.616	0.642	0.616	0.560	0.540	0.552	0.540	0.587	0.602	0.623	0.624	0.557
Zn	0.003	0.003	0.001	0.000	0.001	0.001	0.003	0.002	0.001	0.001	0.002	0.002	0.003	0.002	0.002	0.000	0.001	0.002	0.002
Σcation	3.000	3.000	3.000	3.000	3.000	3.000	3.000	3.000	3.000	3.000	3.000	3.000	3.000	3.000	3.000	3.000	3.000	3.000	3.000
ΣO	4.000	4.000	4.000	4.000	4.000	4.000	4.000	4.000	4.000	4.000	4.000	4.000	4.000	4.000	4.000	4.000	4.000	4.000	4.000
Mg #	57.3	57.6	48.7	50.9	67.3	62.3	47.3	61.5	64.1	61.6	55.0	50.8	55.7	54.1	58.8	60.6	62.7	62.8	51.4
Cr #	86.5	85.1	79.7	87.2	88.6	88.8	89.2	88.1	61.7	89.0	88.5	87.3	82.5	69.2	55.2	87.2	87.9	78.4	88.6

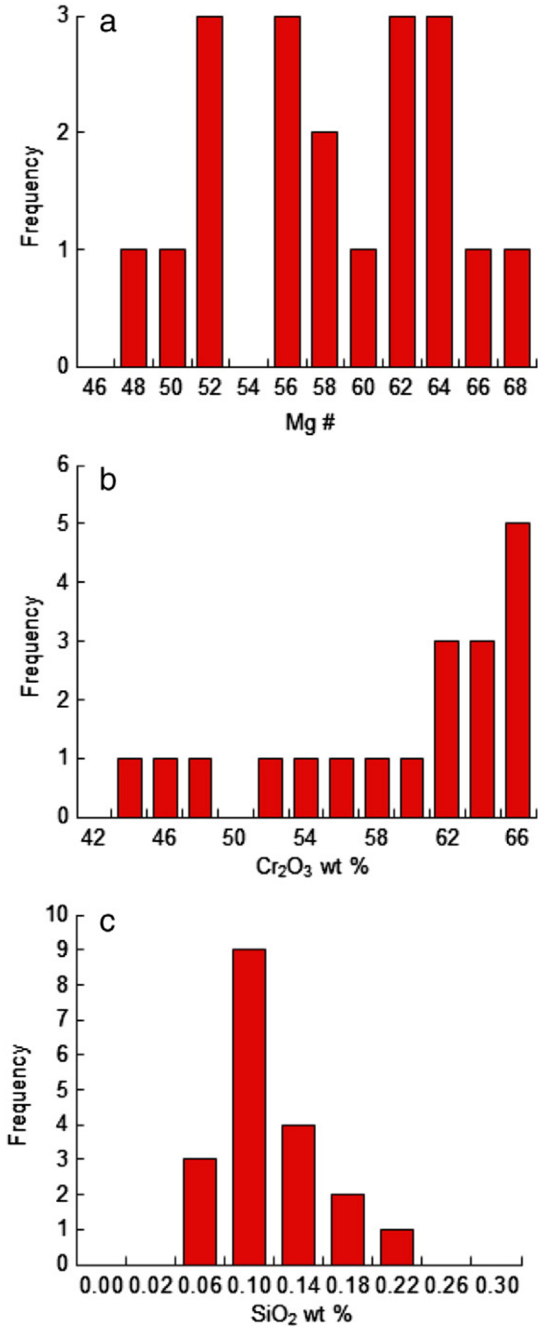

Fig. 8. Histograms of chromite host populations from the No 42 and 50 kimberlite diatremes, Liaoning. a) Mg #, b) Cr_2O_3 wt.% contents, and c) SiO_2 wt.% contents. Mg # = 100Mg / (Mg + Fe^{2+}) by atom in chromite; in all other phases, Fe includes both Fe^{2+} and Fe^{3+}. The data are listed in Table 1.

However, the sulfide inclusion in chromite contains generally higher Fe and lower Ni contents than the corresponding elements in sulfide inclusions in diamond, while Cu in the sulfide inclusion in chromite is less variable than Cu in sulfide inclusions in diamond.

5. Discussion

5.1. Types of mineral inclusions in chromite

The mineral inclusions in chromite include discrete or single mineral inclusions and composite inclusions. There are four distinctive groups of mineral inclusions in terms of mineral species. In decreasing abundance, these mineral inclusions are (1) anhydrous silicate, e.g., olivine and

Table 2
Compositions of olivine inclusions in chromites from the Wafangdian kimberlites. Mg # = 100Mg / (Fe + Mg) by atoms.

Sample	LN42SP01	LN42SP01	LN42SP02	LN42SP02	LN42SP11	LN42SP13	LN42SP14	LN42SP16	LN50SP02	LN50SP03	LN50SP04	LN50SP06	LN50SP11	LN50SP12	LN50SP13
Grain	Ol1	Ol2	Ol1	Ol2											
SiO_2	40.38	41.31	40.23	40.34	39.58	40.91	40.57	39.89	41.01	39.56	40.98	40.54	41.23	41.50	41.06
TiO_2	0.02	0.00	0.00	0.01	0.02	0.00	0.01	0.01	0.01	0.03	0.02	0.02	0.01	0.00	0.04
Al_2O_3	0.03	0.01	0.02	0.02	0.03	0.06	0.02	0.01	0.01	0.01	0.02	0.01	0.01	0.08	0.01
TFeO	8.64	7.49	9.07	8.84	11.25	6.62	7.58	10.87	6.88	9.42	8.60	8.62	7.29	6.59	6.57
NiO	0.35	0.36	0.32	0.36	0.22	0.36	0.40	0.36	0.40	0.42	0.42	0.44	0.41	0.39	0.39
MnO	0.12	0.12	0.15	0.13	0.12	0.09	0.11	0.15	0.09	0.11	0.12	0.12	0.11	0.05	0.07
MgO	49.48	50.66	48.58	48.81	46.99	52.20	50.83	48.59	50.59	50.16	49.73	50.32	51.10	51.56	51.48
CaO	0.03	0.01	0.02	0.02	0.04	0.02	0.02	0.02	0.02	0.05	0.06	0.02	0.02	0.01	0.02
Σ	99.05	99.95	98.38	98.53	98.24	100.27	99.54	99.91	99.00	99.76	99.96	100.09	100.17	100.20	99.62
Si	0.994	1.003	1.000	1.001	0.994	0.984	0.988	0.982	1.003	0.967	1.001	0.987	0.998	1.001	0.996
Al	0.001	0.000	0.001	0.001	0.001	0.002	0.001	0.000	0.000	0.000	0.001	0.000	0.000	0.002	0.000
Ti	0.000	0.000	0.000	0.000	0.000	0.000	0.000	0.000	0.000	0.001	0.000	0.000	0.000	0.000	0.001
Fe	0.178	0.152	0.189	0.183	0.236	0.133	0.154	0.224	0.141	0.192	0.176	0.176	0.148	0.133	0.133
Ni	0.007	0.007	0.006	0.007	0.004	0.007	0.008	0.007	0.008	0.008	0.008	0.009	0.008	0.008	0.008
Mn	0.002	0.002	0.003	0.003	0.003	0.002	0.002	0.003	0.002	0.002	0.003	0.003	0.002	0.001	0.001
Mg	1.816	1.834	1.801	1.805	1.760	1.872	1.846	1.783	1.845	1.828	1.810	1.825	1.844	1.854	1.861
Ca	0.001	0.000	0.000	0.000	0.001	0.000	0.000	0.000	0.001	0.001	0.002	0.001	0.001	0.000	0.000
Σcation	3.000	3.000	3.000	3.000	3.000	3.000	3.000	3.000	3.000	3.000	3.000	3.000	3.000	3.000	3.000
ΣO	3.995	4.004	4.001	4.001	3.995	3.985	3.989	3.982	4.004	3.968	4.001	3.987	3.998	4.002	3.996
Mg #	91.1	92.3	90.5	90.8	88.2	93.4	92.3	88.8	92.9	90.5	91.2	91.2	92.6	93.3	93.3

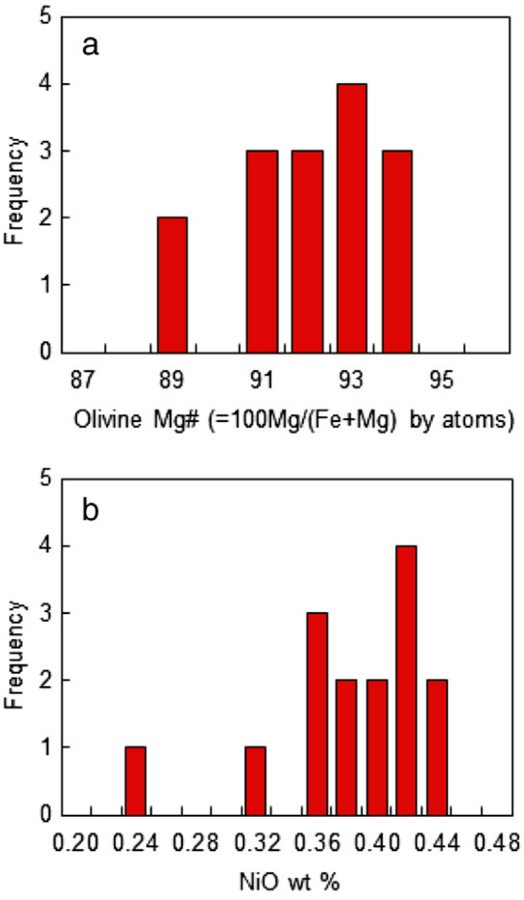

Fig. 9. Histograms of olivine inclusion populations from the No 42 and 50 kimberlite diatremes. a) Mg #, and b) NiO wt.% contents.

garnet, approximately 52% of all inclusions; (2) carbonate, e.g., magnesite, calcium carbonate, dolomite and norsethite, approximately 24%; (3) hydrous silicate, e.g., phlogopite and talc, approximately 12%; (4) sulfide, e.g., pyrrhotite, approximately 3%; and (5) composite inclusions, approximately 9% (Zhao, 1998). The mineral inclusions in chromite belong to the peridotitic suite, similar to peridotitic suite inclusions in diamonds (Harte et al., 1980) and mineral associations in kimberlite (Huang et al., 1992). Some mineral inclusions in chromite are characterized by high volatile components such as H_2O and CO_2.

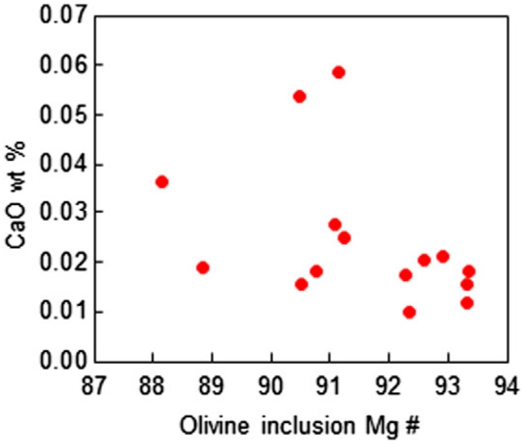

Fig. 10. Mg # versus CaO wt.% contents for the olivine inclusions in chromite from the No. 50 and No. 42 kimberlite diatremes.

Table 3
Compositions of a pyrope inclusion in chromite and its symplectitic pyroxenes (LN42SP01). Mg # = 100Mg / (Fe + Mg), Ca # = 100Ca / (Ca + Mg), both by atoms.

Mineral point	Pyrope average	Pyroxene 6-1	Pyroxene 6-2	Pyroxene 7	Pyroxene 11	Pyroxene 25	Pyroxene 26
SiO_2	40.67	47.85	46.13	49.34	47.61	48.04	47.36
TiO_2	0.05	0.00	0.02	0.00	0.02	0.06	0.02
Al_2O_3	16.70	10.52	11.00	8.78	10.24	8.62	8.32
Cr_2O_3	9.32	4.89	6.39	3.25	4.31	3.58	4.13
TFeO	7.10	7.04	6.87	6.85	4.39	4.03	4.64
NiO		0.00	1.62	1.91	0.63	1.43	0.93
MnO	0.26	0.23	0.20	0.16	0.12	0.16	0.20
MgO	18.30	27.65	27.29	27.96	18.07	15.98	17.38
CaO	7.43	1.38	1.25	1.90	15.23	17.48	14.56
Na_2O	0.02	0.02	0.02	0.03	0.04	0.02	0.02
Σ	99.84	99.58	100.79	100.19	100.66	99.40	97.55
Fe_2O_3	1.00	1.34	4.20	2.53	0.10	0.00	0.00
FeO	6.20	5.84	3.08	4.58	4.30	4.03	4.64
Σ	99.94	99.71	101.21	100.44	100.67	99.40	97.55
Si	2.980	1.695	1.627	1.740	1.720	1.774	1.774
Al iv	0.020	0.305	0.373	0.260	0.280	0.226	0.226
Al vi	1.423	0.134	0.084	0.104	0.156	0.149	0.141
Fe^{+3}	0.055	0.036	0.112	0.067	0.003	0.000	0.000
Ti	0.003	0.000	0.001	0.000	0.000	0.002	0.000
Cr	0.540	0.137	0.178	0.091	0.123	0.105	0.122
Fe^{+2}	0.380	0.173	0.091	0.135	0.130	0.124	0.145
Ni		0.000	0.046	0.054	0.018	0.042	0.028
Mn	0.016	0.007	0.006	0.005	0.004	0.005	0.006
Mg	1.999	1.460	1.434	1.470	0.973	0.880	0.970
Ca	0.583	0.052	0.047	0.072	0.590	0.692	0.584
Na	0.002	0.001	0.001	0.002	0.003	0.001	0.002
Σcation	8.000	4.000	4.000	4.000	4.000	4.000	4.000
ΣO	12.000	6.000	6.000	6.000	6.000	6.015	6.019
Mg #	84.0	87.5	87.6	87.9	88.0	87.6	87.0
Ca #	22.6	3.5	3.2	4.7	37.7	44.0	37.6

5.2. Fluorescence effect of olivine–chromite pair

The Cr_2O_3 content of olivine inclusions in chromite is difficult to obtain due to the fluorescence effect from the chromite host (Cherniak et al., 2010; Llovet and Galan, 2003; Zhao, 1998). The effect of secondary X-ray fluorescence is very pronounced for the pair olivine–chromite. Although the electron beam–sample interaction volume is limited to a few microns, the fluorescence volume, in which secondary X-ray fluorescence occurs, is much larger. When the interaction volume or fluorescence volume crosses a phase boundary, fluorescence corrections of the matrix effects for quantitative analysis may not be correct. For chromite–olivine pairs studied, analyses of Cr_2O_3 concentrations in tiny olivine inclusions in the chromite host could be affected by the secondary fluorescence effect (Zhao, 1998). When the electron beam bombards the olivine, the primary Fe Kα X-ray generated from the olivine will penetrate into a much larger fluorescence volume and may cross the olivine–chromite grain boundary. Since the chromite host has a high Cr_2O_3 concentration and the Cr's critical ionization energy (5.989 keV) is slightly lower than the energy of Fe Kα X-rays (6.403 keV), the Cr in the chromite will be excited by the primary Fe Kα X-rays and secondary Cr Kα X-rays will be generated from the chromite host and be detected as from the olivine inclusion. Therefore, the secondary fluorescence of Cr Kα in chromite by the Fe Kα from olivine will dramatically increase the apparent Cr_2O_3 concentration of the olivine inclusion, making a correction of Cr_2O_3 concentration in the olivine necessary to account for this effect. Fig. 11 shows that the apparent increase in Cr_2O_3 concentration from the center of the olivine inclusion to the olivine–chromite boundary, illustrating that the apparent Cr_2O_3 concentration could be artificially increased even at the center of an olivine inclusion of 50 μm in size. The secondary fluorescence effect is more pronounced for the same sample analyzed at 30 kV. To remove the effect of secondary fluorescence, the olivine inclusion was removed from the chromite host and analyzed, which results in Cr_2O_3 concentrations for the olivine inclusion of ~0.10 ± 0.02 wt.%. Therefore, the phase boundary fluorescence effect must be considered when small mineral inclusions are analyzed by electron microprobe, as well as when performing analyses near interfaces where there are compositional differences and the potential for secondary excitation.

5.3. Symplectitic rim of a pyrope inclusion in chromite

There is a symplectitic rim surround a pyrope inclusion in a chromite (LN42SP01). From the chemical compositions determined by EPMA (Table 3), chemical formulae of the phases involved are calculated as pyrope $(Mg,Ca,Fe^{2+})(Al,Cr)_2Si_3O_{12}$, clinopyroxene $(Mg,Ca,Fe^{2+},Al,Cr)_2(Si,Al)_2O_6$, a second pyroxene $(Mg,Fe^{2+},Ca,Al,Cr,Fe^{3+})_2(Si,Al)_2O_6$, and spinel $MgAl_2O_4$. Giving the ubiquity of olivine in the mantle and in the chromites studied, reaction garnet + olivine = pyroxenes + spinel could have been involved in the formation of the symplectitic rim. Thus, the symplectitic rim may have formed as a result of reaction of the garnet with olivine before being included by the chromite host. A second possibility is that the symplectitic rim formed as products of the breakdown or decomposition of the pyrope at lower pressures during its transportation from its stable region (Mitchell, 1986). Garvie and Robinson (1982) suggested that typical kelyphite formed on garnet at 900°–1300 °C and 10–20 kbar. It may also possible that the symplectitic rim formed by melting of garnet during decompression, with the minerals in the symplectite subsequently crystallizing from the liquid.

5.4. Composite inclusions in chromite and kimberlitic magma

The composite inclusion in chromite LN50SP07 contains by exposed surface area approximately 25% magnesite, 25% dolomite, 5% norsethite, 20% phlogopite, and 25% of a pure SiO_2 phase. Based on the above mineral mode and the chemical compositions (Tables 5 and 7), bulk composition of the composite inclusion is calculated as SiO_2 33.2 wt.%, Al_2O_3 2.5 wt.%, MgO 22.0 wt.%, CaO 7.5 wt.%, BaO 2.5 wt.%, K_2O 0.8 wt.%, CO_2 25.5 wt.%, and H_2O 0.8 wt.%. In the calculation of the bulk composition of the composite inclusion, the composition of a discrete phlogopite inclusion from chromite LN42SP07 was used (Fig. 7a; Table 4) as the phlogopite in the composite inclusion in sample LN50SP07 is too small and has poor conductivity and attempt to obtain its chemical composition was unsuccessful. However, it is a good approximation to use the composition of this discrete phlogopite inclusion in calculation of the bulk composition, as the discrete phlogopite inclusion in sample LN42SP07 is similar in chemical composition to those in mantle xenoliths and in kimberlite (Section 4.3) and is likely similar to the phlogopite in sample LN50SP07 too. The SiO_2, Al_2O_3, MgO, CaO and K_2O contents of the calculated bulk composition are well within the compositional range of the Wafangdian kimberlite (Huang et al., 1992), although the CO_2 and BaO are higher and the H_2O is lower. The high calculated BaO content are due to norsethite, which contains 46.84 wt.% to 50.28 wt.% BaO (Table 6). Mitchell (1994) reported a Ca–Ba carbonate found in the groundmass of the Benfontein calcite kimberlite, South Africa. The compositional similarity

Table 4
Compositions of a phlogopite inclusion in chromite (LN42SP07). Mg # = 100Mg / (Mg + Fe^{+2} + Fe^{+3}) by atoms.

Point	1	2	3	4	5	6	7	8	9	10	11	Ave
SiO_2	39.76	40.83	41.67	41.15	40.84	40.79	38.96	39.79	39.97	44.55	40.56	40.81
TiO_2	0.22	0.15	0.74	0.37	0.25	0.42	0.37	0.27	0.34	0.31	0.56	0.36
Al_2O_3	12.61	12.91	12.93	12.15	12.31	12.51	11.78	11.91	12.02	13.00	12.24	12.40
Cr_2O_3	2.19	2.32	2.37	2.22	2.26	2.48	2.30	2.20	2.10	1.97	2.28	2.24
FeOt	5.96	5.80	5.82	5.63	5.48	5.68	4.96	4.84	5.19	5.45	5.32	5.47
NiO	0.28	0.56	0.15	0.61	0.58	0.03	0.53	0.56	0.13	0.00	0.00	0.31
MnO	0.07	0.00	0.00	0.00	0.00	0.15	0.00	0.09	0.00	0.11	0.00	0.04
MgO	25.12	25.36	25.68	24.66	25.11	25.21	22.57	24.42	23.82	25.37	25.57	24.81
CaO	0.00	0.01	0.00	0.02	0.01	0.01	0.00	0.05	0.00	0.04	0.02	0.01
BaO	0.00	0.00	0.04	0.00	0.00	0.00	0.00	0.00	0.04	0.00	0.00	0.01
Na_2O	0.01	0.01	0.03	0.01	0.00	0.00	0.00	0.00	0.02	0.00	0.00	0.01
K_2O	3.15	2.78	4.34	4.05	3.68	3.31	5.44	4.27	3.97	2.42	3.99	3.76
F	0.56	0.50	0.47	0.44	0.41	0.47	0.23	0.42	0.36	0.43	0.49	0.43
Cl	0.03	0.03	0.06	0.05	0.03	0.03	0.04	0.03	0.05	0.05	0.05	0.04
Σ	89.96	91.26	94.30	91.36	90.96	91.09	87.18	88.85	88.01	93.70	91.08	90.70
Fe_2O_3	6.62	6.45	6.47	6.26	6.09	6.31	5.51	5.38	5.77	6.06	5.91	6.08
FeO	0.00	0.00	0.00	0.00	0.00	0.00	0.00	0.00	0.00	0.00	0.00	0.00
H_2O	4.56	4.76	4.16	4.04	4.31	4.44	3.87	3.93	3.93	4.50	4.20	4.13
O═F	−0.24	−0.21	−0.20	−0.19	−0.17	−0.20	−0.10	−0.18	−0.15	−0.18	−0.21	−0.18
O═Cl	−0.01	−0.01	−0.01	−0.01	−0.01	−0.01	−0.01	−0.01	−0.01	−0.01	−0.01	−0.01
Σ	94.94	96.45	98.89	95.83	95.70	95.95	91.49	93.14	92.35	98.62	95.66	95.26
# of ions												
Si	5.612	5.659	5.687	5.797	5.734	5.694	5.860	5.763	5.830	5.990	5.691	5.756
Al iv	2.098	2.109	2.080	2.017	2.037	2.058	2.088	2.033	2.066	2.010	2.024	2.061
Al vi	0.000	0.000	0.000	0.000	0.000	0.000	0.000	0.000	0.000	0.050	0.000	0.000
Ti	0.023	0.016	0.076	0.039	0.026	0.044	0.042	0.029	0.037	0.031	0.059	0.039
Cr	0.244	0.254	0.256	0.247	0.251	0.274	0.274	0.252	0.242	0.209	0.253	0.250
Fe^{+3}	0.704	0.672	0.664	0.663	0.643	0.663	0.624	0.586	0.633	0.613	0.624	0.645
Fe^{+2}	0.000	0.000	0.000	0.000	0.000	0.000	0.000	0.000	0.000	0.000	0.000	0.000
Ni	0.026	0.051	0.014	0.057	0.054	0.003	0.053	0.054	0.013	0.000	0.000	0.029
Mn	0.008	0.000	0.000	0.000	0.000	0.018	0.000	0.011	0.000	0.013	0.000	0.005
Mg	5.285	5.239	5.224	5.178	5.255	5.246	5.060	5.272	5.179	5.084	5.348	5.216
Ca	0.000	0.001	0.000	0.003	0.002	0.001	0.000	0.008	0.000	0.006	0.003	0.002
Ba	0.000	0.000	0.002	0.000	0.000	0.000	0.000	0.000	0.002	0.000	0.000	0.000
Na	0.003	0.003	0.008	0.003	0.000	0.000	0.000	0.000	0.006	0.000	0.000	0.002
K	0.567	0.491	0.756	0.728	0.659	0.589	1.044	0.789	0.739	0.415	0.714	0.677
A site	0.570	0.496	0.766	0.734	0.661	0.591	1.044	0.797	0.747	0.421	0.717	0.682
Mg #	88.3	88.6	88.7	88.6	89.1	88.8	89.0	90.0	89.1	89.2	89.5	89.0

Table 5
Compositions of a talc inclusion in chromite (LN50SP01). Mg # = 100Mg / (Fe + Mg) by atoms. Based on talc $3MgO \cdot 4SiO_2 \cdot H_2O$, normalized to 11 O.

Position	1 (core)	2	3	4 (rim)	Average
SiO_2	59.60	59.16	56.90	57.35	58.25
TiO_2	0.01	0.00	0.02	0.01	0.01
Al_2O_3	0.32	0.43	0.87	1.11	0.68
Cr_2O_3	0.55	0.71	0.60	0.92	0.70
FeO	4.17	4.22	4.10	3.86	4.09
NiO	0.17	0.04	0.09	0.18	0.12
MnO	0.00	0.00	0.02	0.00	0.01
MgO	28.41	27.78	26.08	26.74	27.25
CaO	0.02	0.01	0.03	0.02	0.02
Σ	93.24	92.36	88.71	90.19	91.12
H_2O	4.54	4.49	4.32	4.39	4.43
Σ	97.77	96.85	93.03	94.58	95.56
Si	3.940	3.946	3.949	3.919	3.939
Al	0.025	0.034	0.071	0.089	0.054
Ti	0.000	0.000	0.001	0.000	0.000
Cr	0.029	0.038	0.033	0.050	0.037
Fe	0.230	0.235	0.238	0.221	0.231
Ni	0.007	0.002	0.004	0.008	0.005
Mn	0.000	0.000	0.001	0.000	0.000
Mg	2.800	2.762	2.698	2.723	2.747
Ca	0.001	0.001	0.002	0.001	0.001
Σcation	7.033	7.018	6.998	7.011	7.015
ΣO	11.000	11.000	11.000	11.000	11.000
Mg #	92.4	92.2	91.9	92.5	92.2

between the composite inclusion and the kimberlite host rock suggests that the inclusion represents crystallized products of a trapped kimberlitic magma. This further implies that the host chromite crystal crystallized from kimberlitic magma, and that the kimberlitic magma was trapped initially as a melt inclusion and then crystallized as a composite inclusion in the chromite host. The existence of carbonates and hydrous silicate in the composite inclusions suggests that volatile components in the C–O–H system were involved in the formation of kimberlitic magma, probably in the form of metasomatism-invoked partial melting of a depleted mantle source. This could represent a metasomatic event during the later stage of diamond growth in solid state environment as indicated by a mica–orthopyroxene–rutile–ilmenite–diopside ± chromite (MORID by Zhao et al., 1999).

5.5. *Pressure and temperature inferred from chromite and its mineral inclusions*

Logvinova and Sobolev (1991, 1995) have estimated the P–T for inclusion assemblages in kimberlitic chromite. Due to differential compressibility and thermal expansivity, the pressure in an inclusion may not be the same as the host pressure (Zhang, 1998). Thus, estimation of P and T could be complicated if the physical conditions have changed after the formation of host–inclusion assemblage. The complexity may be avoided by using initial compositions of inclusion and host at formation (Wang et al., 1999; Zhang, 1998). Composition of an inclusion in a chromite host, e.g., olivine, may have been altered after incorporation in chromite. In Fig. 12, an olivine inclusion in chromite (LN50SP01) shows a U-shape profile for Fe across the olivine grain. The Fe content is relatively constant in the core area of the profile and is elevated toward the olivine inclusion–chromite host boundaries. This suggests that the initial composition of the olivine may have been preserved in the core area of the olivine inclusion, while the elevated Fe content approaching to the rim of the olivine inclusion has altered either through diffusion with the host chromite or by detecting some Fe in the chromite host if the olivine inclusion is thin enough below the polished surface. Therefore, the core composition of the olivine inclusion in the chromite may provisionally be used to obtain P–T of formation. For an inclusion of small size, even the original core composition could be altered. If this is the case, restoration of initial composition of an inclusion is necessary in order to obtain reliable P–T conditions of formation (Wang et al., 1999). Composition of a chromite host distant from the inclusion–host boundary is not expected to be changed by compositional exchange between inclusion and host, because the volume of the chromite host is much larger than that of the inclusion. In this study, P–T of formation was obtained using the unaltered core composition of an inclusion and the composition of its chromite host away from the inclusion–host boundary.

Table 6
Compositions of carbonate inclusions in chromite from the No. 42 and 50 kimberlites. The CO_2 is calculated by stoichiometry.

Sample #	LN42SP07	LN50SP05	LN50SP07-1	LN42SP06-1	LN50SP07-3	LN50SP07-4	LN42SP06-3	LN50SP07-5
Mineral	Ca-carbonate	Magnesite	Magnesite	Dolomite	Dolomite	Dolomite	Norsethite	Norsethite
Average	4	8	5	1	4	2	2	Ave
CaO	54.98	1.27	0.10	29.12	30.57	29.75	0.26	1.05
MgO	0.31	43.71	44.19	19.79	20.46	21.43	10.43	12.24
MnO	0.18	0.11	0.07	0.10	0.10	0.01	0.00	0.01
FeO	0.27	3.74	0.41	1.61	0.63	0.59	1.62	2.01
SrO	0.02	0.01	0.00	0.50	0.35	0.38	0.05	0.10
BaO	0.02	0.01	0.03	0.00	0.01	0.08	46.84	50.28
CO_2	43.78	51.08	48.63	45.72	46.92	47.30	26.05	29.89
Σ	99.57	99.91	93.43	96.83	99.03	99.54	85.25	95.58
# of ions								
Ca	1.971	0.039	0.003	1.000	1.023	0.987	0.016	0.055
Mg	0.015	1.869	1.984	0.945	0.952	0.989	0.874	0.894
Mn	0.005	0.003	0.002	0.003	0.003	0.000	0.000	0.000
Fe	0.008	0.090	0.010	0.043	0.016	0.015	0.076	0.082
Sr	0.000	0.000	0.000	0.009	0.006	0.007	0.002	0.003
Ba	0.000	0.000	0.000	0.000	0.000	0.001	1.032	0.966
C	2.000	2.000	2.000	2.000	2.000	2.000	2.000	2.000
O	6.000	6.000	6.000	6.000	6.000	6.000	6.000	6.000
% molecule								
$CaCO_3$	98.6	1.9	0.2	50.0	51.1	49.4	0.8	2.7
$MgCO_3$	0.8	93.4	99.2	47.3	47.6	49.5	43.7	44.7
$MnCO_3$	0.3	0.1	0.1	0.1	0.1	0.0	0.0	0.0
$FeCO_3$	0.4	4.5	0.5	2.2	0.8	0.8	3.8	4.1
$SrCO_3$	0.0	0.0	0.0	0.5	0.3	0.3	0.1	0.1
$BaCO_3$	0.0	0.0	0.0	0.0	0.0	0.0	51.6	48.3
Σ	100.0	100.0	100.0	100.0	100.0	100.0	100.0	100.0

Table 7
Compositions of a sulfide inclusion in chromite (LN50-SP10). Note: po: pyrrhotite Fe_7S_8 to Fe_8S_8; grg: greigite Fe_3S_4.

Phase	po	grg?	grg?	grg?	po	grg?	grg?	po	po	po	grg?	
Analysis	1	2	3	4	5	6	11	12	13	14	15	Ave
Fe	45.45	56.20	57.25	54.00	50.82	54.17	34.01	48.05	48.22	55.69	49.88	50.34
Ni	9.00	0.52	1.17	3.17	6.70	3.03	24.25	10.78	10.77	1.97	6.54	7.08
Cu	5.62	2.13	0.62	2.06	2.47	1.98	0.85	2.18	1.94	1.87	1.98	2.15
Zn	0.03	0.01	0.01	0.00	0.00	0.00	0.03	0.04	0.00	0.05	0.01	0.01
Mn	0.00	0.00	0.00	0.00	0.00	0.00	0.00	0.00	0.00	0.00	0.00	0.00
Co	0.05	0.00	0.00	0.02	0.12	0.05	0.67	0.15	0.11	0.00	0.15	0.12
S	38.21	41.70	41.35	41.69	41.06	41.92	42.01	39.90	39.03	41.20	42.17	40.93
S	98.35	100.56	100.40	100.93	101.16	101.15	101.82	101.09	100.06	100.78	100.72	100.64
Sulfur normalized to 4												
Fe	2.731	3.095	3.179	2.974	2.843	2.967	1.859	2.766	2.837	3.104	2.716	2.824
Ni	0.514	0.027	0.062	0.166	0.356	0.158	1.261	0.590	0.603	0.104	0.339	0.378
Cu	0.297	0.103	0.030	0.100	0.121	0.095	0.041	0.110	0.100	0.092	0.095	0.106
Zn	0.001	0.000	0.000	0.000	0.000	0.000	0.001	0.002	0.000	0.002	0.000	0.001
Mn	0.000	0.000	0.000	0.000	0.000	0.000	0.000	0.000	0.000	0.000	0.000	0.000
Co	0.003	0.000	0.000	0.001	0.006	0.003	0.035	0.008	0.006	0.000	0.008	0.006
S	4.000	4.000	4.000	4.000	4.000	4.000	4.000	4.000	4.000	4.000	4.000	4.000
Scation	3.547	3.225	3.272	3.240	3.327	3.223	3.197	3.476	3.546	3.303	3.157	3.315

For the chromite–olivine–garnet assemblage (LN42SP01), an olivine–garnet Fe–Mg thermometer (O'Neill, 1980; O'Neill and Wood, 1979), two versions of olivine–spinel thermometers (Ballhaus et al., 1991; O'Neill and Wall, 1987), and a garnet–olivine–spinel–orthopyroxene barometer (Webb and Wood, 1986) were applied to calculated temperatures at an assumed pressure range of 30–70 kbar and pressures at an assumed temperature range of 500°–1300 °C (Fig. 13a). The pressure from the garnet–olivine–spinel–orthopyroxene barometer is a lower limit due to absence of orthopyroxene. Therefore, the actual pressure is at the right side of the curve for the garnet–olivine–spinel–orthopyroxene barometer (Fig. 13a). The temperatures from the two olivine–spinel thermometers used match very well. However, the olivine–garnet Fe–Mg thermometer for the chromite–olivine–garnet assemblage gives higher temperatures than olivine–spinel thermometry. If combination of the garnet–olivine–spinel–orthopyroxene barometer and the olivine–garnet thermometer are used, the calculated pressure and temperature are approximately >53 kbar and 1130 °C; if the garnet–olivine–spinel–orthopyroxene barometer and the olivine–spinel thermometer are selected, the calculated pressure and temperature would be approximately >46 kbar and 980 °C (Fig. 13a). Nevertheless, both P–Ts are within the stability field of diamond, indicating that the kimberlitic chromite came from a depth of ~150 km.

Two olivine–spinel thermometers (Ballhaus et al., 1991; O'Neill and Wall, 1987) yield similar temperatures for some olivine–spinel pairs (Fig. 13b and c). But for some other olivine–spinel pairs, the thermometer of Ballhaus et al. (1991) generally yields higher temperatures than that of O'Neill and Wall (1987). For example, in samples LN42SP13, both thermometers yield significantly different results (Fig. 13d). Sample LN50SP04 contains much lower Cr_2O_3 (~45 wt.%). At 50 kbar, temperatures obtained from olivine–spinel pairs are from 950° to 1130 °C (O'Neill and Wall, 1987) or from 1000° to 1290 °C (Ballhaus et al., 1991).

6. Summary

Electron probe microanalysis and microscopy techniques are widely used tools for investigating and characterizing minerals associated with mineral deposits. Signals generated in an electron probe instrument provide information on chemistry and image of a sample at micro- and nano-scale. Mineral inclusions in chromite from the Wafangdian kimberlite, Liaoning Province, China are similar to the mineral inclusions in diamond from the same location and they are also major or common components of kimberlite. They include anhydrous silicates, hydrous silicates, carbonates, and sulfides. Chemical compositions of the chromite hosts vary in Cr_2O_3 from 42 to 66 wt.% and Mg # of 47 to 67. One chromite contains two olivine inclusions and one garnet inclusion. The garnet inclusion has a symplectitic rim of aluminous orthopyroxene, clinopyroxene, and spinel, which probably formed before being included in chromite host. Applications of an olivine–garnet thermometer, two olivine–spinel thermometer, and an orthopyroxene–spinel–garnet–olivine barometer to the chromite–garnet–pyroxene–olivine assemblage yields a pressure and temperature range of 46 kbar and 980 °C to 53 kbar and 1130 °C, within the stability

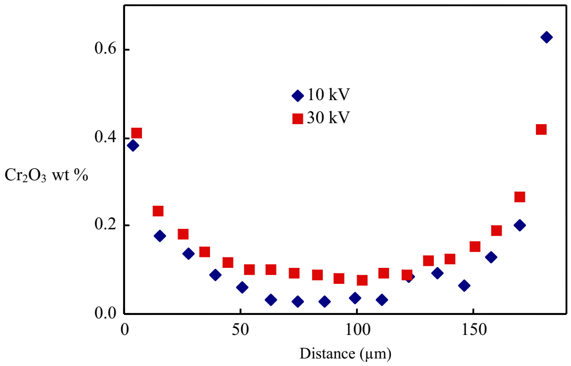

Fig. 11. Variations of Cr content across an olivine inclusion inside the chromite host LN50SP06. Analyzed by EPMA at 10 and 30 kV, respectively. The increase of Cr toward the chromite–olivine boundary is due to fluorescence effect. The Cr fluorescence effect becomes significant with increasing voltage or approaching the olivine–chromite boundary.

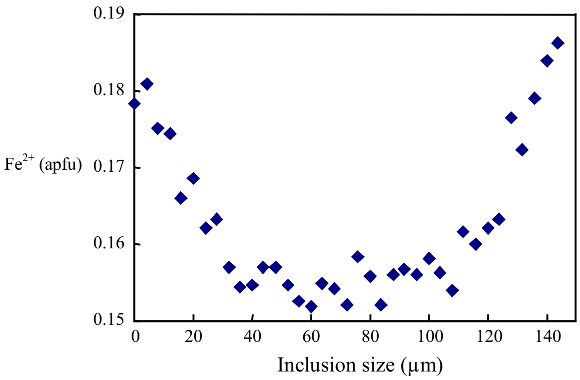

Fig. 12. Fe^{2+} variation across an olivine inclusion in chromite LN42SP01. The Fe content is relatively constant in the core area of the profile and is elevated toward the olivine inclusion–chromite host boundaries.

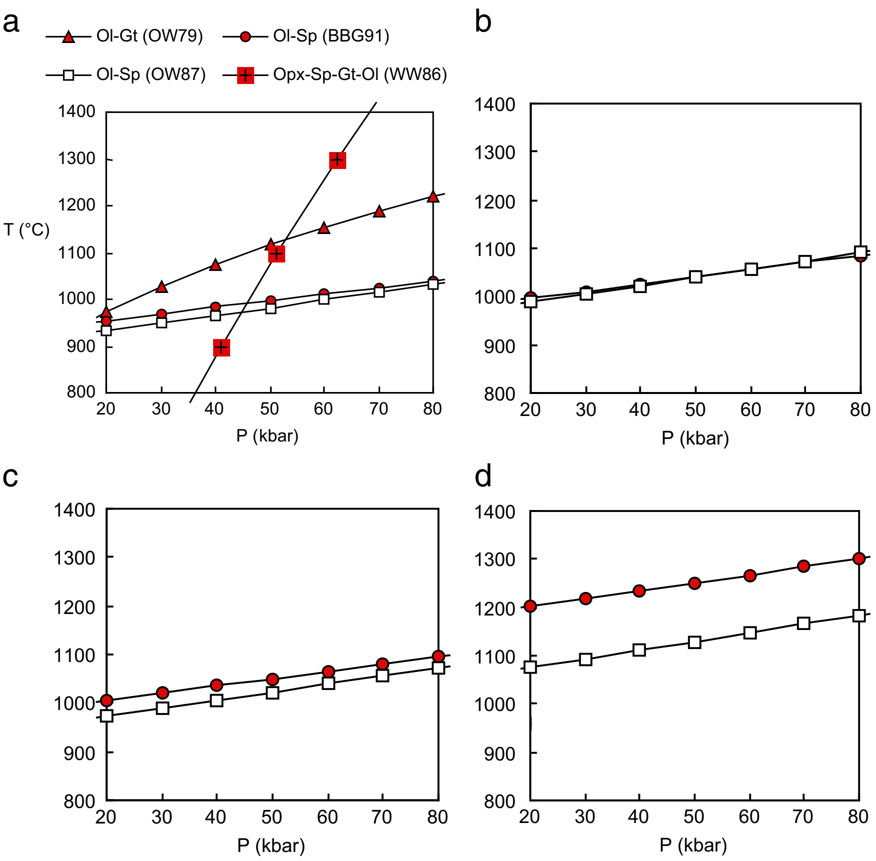

Fig. 13. Pressure–temperature calculated for chromite and its inclusion assemblages from the Wafangdian Kimberlite diatremes. a) Olivine–garnet–spinel for chromite LN42SP01; b) Olivine–spinel for chromite LN42SP02; c) Olivine–spinel for chromite LN50SP02: and d) Olivine–spinel for chromite LN42SP13. Each curve represents a thermobarometer: OW79 — olivine–garnet Fe–Mg thermometer (O'Neill and Wood, 1979); OW87 — olivine–spinel thermometer (O'Neill and Wall, 1987); BBG91 — olivine–spinel thermometer (Ballhaus et al., 1991); and WW86 — garnet–olivine–spinel–orthopyroxene barometer (Webb and Wood, 1986).

field of diamond, suggesting that high Cr chromites can be used as an indication mineral for exploration of diamond and kimberlite. A rare mineral, norsethite $BaMg(CO_3)_2$, was discovered in several chromite grains from both the No. 50 and the No. 42 diatremes. A composite inclusion of magnesite, dolomite, norsethite, phlogopite, and a SiO_2 phase in a chromite has a bulk composition of 33.2 wt.% SiO_2, 2.5 wt.% Al_2O_3, 22.0 wt.% MgO, 7.5 wt.% CaO, 2.5 wt.% BaO, 0.8 wt.% K_2O, 25.5 wt.% CO_2, and 0.8 wt.% H_2O. This composition is similar to the chemical composition of the Wafangdian kimberlite, suggesting that the composite inclusion represents trapped kimberlitic magma. While discrete inclusions, such as olivine and garnet, were mostly likely trapped as crystals, the composite silicate + carbonate inclusions may represent trapped kimberlitic magma. The wide and diverse chemical compositions of the chromite and its mineral inclusions suggest a multiple origin of chromites in the kimberlite.

Conflict of interest

There is no conflict of interest.

Acknowledgments

This study was supported by funding from NSF (EAR 93-15918, 94-58368, 97-25566, 91-17772, 95-26596), NWT Geology Division of DIAND of the Government of Canada, the Geological Society of America, the University of Michigan, and the Jackson School of Geosciences at the University of Texas at Austin. The field trip was sponsored by the Institute of Mineral Deposits of Chinese Academy of Geological Sciences and the Liaoning Sixth Geological Team. Yunhui Huang, Shuying Qin, Yawen Cao, Ruishan Liu, Zhuguo Han, Jize Lin, Qing Miao, Liping Wang, Weixin Wang, and Xianfeng Fu are thanked for providing samples and for assistance for facilitating the field trip. The electron microprobe analyzer used in this work was from the R. B. Mitchell Electron Microbeam Analysis Laboratory at the University of Michigan and was acquired under Grant # EAR82-12764 from the National Science Foundation. We are grateful to Douglas Smith for his very helpful comments on an earlier version of this manuscript.

References

Armstrong, J.T., 1988. Bence–Albee after 20 years: review of the accuracy of α-factor correction procedures for oxide and silicate minerals. In: Newbury, D.E. (Ed.), Microbeam Analysis, pp. 469–476.

Armstrong, J.T., 1991. Quantitative elemental analysis of individual microparticles with electron beam instruments. In: Heinrich, K.F.J., Newbury, D.E. (Eds.), Electron Probe Quantitation. Plenum, New York, pp. 261–315.

Armstrong, J.T., 1995. CITZAF: a package of correction programs for the quantitative electron microbeam X-ray-analysis of thick polished materials, thin films, and particles. Microbeam Anal. 4, 177–200.

Armstrong, J.T., McSwiggen, P., Mori, N., Nielsen, C., 2013. A thermal field-emission electron probe microanalyzer for improved analytical spatial resolution. Microscopy and Analysis No 128. ,pp. 20–24.

Ballhaus, C., Berry, R.F., Green, D.H., 1991. High pressure experimental calibration of the olivine–orthopyroxene–spinel oxygen geobarometer: implications for the oxidation state of the upper mantle. Contrib. Mineral. Petrol. 107, 27–40.

Bence, A.E., Albee, A.L., 1968. Empirical correction factors for the electron microanalysis of silicates and oxides. J. Geol. 76, 382–403.

Böttcher, M.E., Gehlken, P.L., Skogby, H., Reutel, C., 1997. The vibrational spectra of $BaMg(CO_3)_2$. Mineral. Mag. 61, 249–256.

Brindley, G.W., Bish, D.L., Wan, H.M., 1977. The nature of kerolite, its relation to talc and stevensite. Mineral. Mag. 41, 443–452.

Brown, J.D., 1991. φ(ρz) equations for quantitative analysis. In: Heinrich, K.F.J., Newbury, D.E. (Eds.), Electron Probe Quantitation. Plenum, New York, pp. 77–82.

Carpenter, P.K., 2008. EPMA standards: the good, the bad, and the ugly. Microsc. Microanal. 14 (Suppl. 2), 530–531.

Carpenter, P.K., Vicenzi, E.P., 2012. Mineral reference standards and quantitative electron-probe microanalysis. Microanalytical Reference Materials Topical Conference Abstracts Volume. Microanalysis Society, Golden, Colorado.

Castaing, R., 1951. Application des sondes électroniques à une méthode d'analyse ponctuelle chimique et cristallographique. PhD Thesis, University of Paris, Publication ONERA No. 55.

Cherniak, D.J., Hervig, R., Koepke, J., Zhang, Y., Zhao, D., 2010. Analytical methods in diffusion studies. Rev. Mineral. Geochem. 72, 107–170.

Conty, C., 2001. Today's and tomorrow's instruments. Microsc. Microanal. 7, 142–149.

Dong, Z., 1994. Kimberlites in China. Science Press, Beijing (318 pp.).

Donovan, J.J., Tingle, T.N., 1996. An improved mean atomic number background correction for quantitative microanalysis. JMSA 2, 1–7.

Donovan, J.J., Lowers, H.A., Rusk, B.G., 2011. Improved electron probe microanalysis. Am. Mineral. 96, 274–282.

Essene, E.J., Henderson, C., 1999. Selecting standards to optimize electron microprobe analysis. Microsc. Microanal. 5 (Suppl. 2), 566–567.

Forbes, W.C., 1971. Iron content of talc in the system $Mg_3Si_4O_{10}(OH)_2$–$Fe_3Si_4O_{10}(OH)_2$. J. Geol. 79, 63–74.

Garvie, O.G., Robinson, D.N., 1982. The mineralogy, structure and mode of formation of kelyphite and associated sub-kelyphitic surfaces on pyrope from kimberlite. Terra Cognita 2, 229–230.

Goldstein, J.I., Newbury, D.E., Joy, D.C., Lyman, C.E., Echlin, P., Lifshin, E., Sawyer, L., Michael, J., 2003. Scanning Electron Microscopy and X-ray Microanalysis, third ed. Kluwer Academic/Plenum Publishers, (689 pages).

Goldstein, J.I., Newbury, D.E., Echlin, P., Joy, D.C., Romig Jr., D., Lyman, C.E., Fiori, C., Lifshin, E., 2011. Scanning Electron Microscopy and X-ray Microanalysis, fourth ed. Springer, US (840 pages).

Harte, B., Gurney, J.J., Harris, J.W., 1980. The formation of peridotitic suite inclusions in diamonds. Contrib. Mineral. Petrol. 72, 181–190.

Hombourger, C., Outrequin, M., 2013. Quantitative analysis and high-resolution X-ray mapping with a field emission electron microprobe. Microsc. Today 21, 10–15.

Hoschek, G., 1995. Stability relations and Al content of tremolite and talc in CMASH assemblages with kyanite + zoisite + quartz + H_2O. Eur. J. Mineral. 7, 353–362.

Huang, Yunhui, Qin, Shuying, Zhou, Xiuzhong, Deng, Chujun, Zhao, Donggao, Yang, Jianmin, Guo, Yuemin, Gao, Yan, Li, Gejing, 1992. Kimberlites and Diamonds in the North China Craton (in Chinese). Geological Publishing House, Beijing (206 pp.).

Jarosewich, E., 2002. Smithsonian microbeam standards. J. Res. Natl. Inst. Stand. Technol. 107, 681–685.

Jarosewich, E., Boatner, L.A., 1991. Rare-earth element reference samples for electron microprobe analysis. Geostand. Newslett. 15, 397–399.

Jarosewich, E., MacIntire, I.G., 1983. Carbonate reference samples for electron microprobe and scanning electron microscope analysis. J. Sediment. Petrol. 53, 677–678.

Jarosewich, E., White, J.S., 1987. Strontianate reference sample for electron microprobe and SEM analyses. J. Sediment. Petrol. 57, 762–763.

Jarosewich, E., Nelen, J.A., Norberg, J.A., 1980. Reference samples for electron microprobe analysis. Geostand. Newslett. 4, 43–47.

Jarosewich, E., Gooley, R., Husler, J., 1987. Chromium augite — a new microprobe reference sample. Geostand. Newslett. 11, 197–198.

Jercinovic, M.J., Williams, M.L., 2005. Analytical perils (and progress) in electron microprobe trace element analysis applied to geochronology: background acquisition, interferences, and beam irradiation effects. Am. Mineral. 90, 526–546.

Keil, K., 1967. The electron microprobe X-ray analyzer and its application in mineralogy. Fortschr. Mineral. 44, 4–66.

Kerrick, D.M., Eminhizer, L.B., Villaume, J.F., 1973. The role of carbon film thickness in electron microprobe analysis. Am. Mineral. 58, 920–925.

Knoll, M., Ruska, E., 1932. Z. Phys. 78, 318.

Llovet, X., Galan, G., 2003. Correction of secondary X-ray fluorescence near grain boundaries in electron microprobe analysis: application to thermobarometry of spinel lherzolites. Am. Mineral. 88, 121–130.

Llovet, X., Pinard, P.T., Donovan, J.J., Salvat, F., 2012. Secondary fluorescence in electron probe microanalysis of material couples. J. Phys. D. Appl. Phys. 45, 1–12.

Logvinova, A.M., Sobolev, N.V., 1991. Crystalline inclusions in chromites from kimberlites and lamproite. In: Meyer, H.O.A., Leonardos, O.H. (Eds.), Kimberlites, Related Rocks and Mantle XenolithsProc. Fifth Int. Kimberlite Conf 1. CPRM-Special Publication, Araxa, Brazil, p. 240.

Logvinova, A.M., Sobolev, N.V., 1995. Morphology and composition of mineral inclusions in chromite macrocrysts from kimberlites and lamproite. In: Extended Abstract of the Sixth International Kimberlite Conference 1995, United Institute of Geology, Geophysics and Mineralogy; Novosibirsk, Russia (707 pp.).

Maaskant, P., Kaper, H., 1991. Fluorescence effects at phase boundaries: petrological implications for Fe–Ti oxides. Mineral. Mag. 55, 277–279.

MacRae, C.M., Wilson, N.C., Notoya, S., 2006. Improvements in mapping and microanalysis by FEG-EPMA. Microsc. Microanal. 12 (S2), 1378CD.

Matsukage, K., Arai, S., 1998. Jadeite, albite and nepheline as inclusions in spinel of chromitite from Hess Deep, equatorial Pacific: their genesis and implications for serpentinite diapir formation. Contrib. Mineral. Petrol. 131, 111–122.

McDonald, J.A., 1965. Liquid immiscibility as one factor in chromite seam formation in the Bushveld Igneous Complex. Econ. Geol. 60, 1674–1685.

McGee, J.J., Keil, K., 2001. Application of electron probe microanalysis to the study of geological and planetary materials. Microsc. Microanal. 7, 200–210.

McGuire, A.V., Francis, C.A., Dyar, M.D., 1992. Mineral standards for electron microprobe analysis of oxygen. Am. Mineral. 77, 1087–1091.

McSwiggen, P., 2014. Characterisation of sub-micrometre features with the FE-EPMA. Mater. Sci. Eng. 55, 1–12.

McSwiggen, P., Mori, N., Ohta, T., Nielsen, C., 2012. Low accelerating voltage, X-ray microanalysis: benefits and challenges. Microsc. Microanal. 18 (Suppl. 2), 1042–1043.

McSwiggen, P., Armstrong, J.T., Nielsen, C., 2014. Strategies for low accelerating voltage X-ray microanalysis of sub-micrometer features with the FE-EPMA. Microsc. Microanal. 20 (Suppl. 3), 688–689.

Mitchell, R.H., 1986. Kimberlites: Mineralogy, Geochemistry, and Petrology. Plenum Press, New York and London (442 pp.).

Mitchell, R.H., 1994. Accessory rare earth, strontium, barium and zirconium minerals in the Benfontein and Wesselton calcite kimberlites, South Africa. In: Meyer, H.O.A., Leonardos, O.H. (Eds.), Kimberlites, Related Rocks and Mantle Xenoliths (Proceedings of the Fifth International Kimberlite Conference, 1). CPRM—Special Publication, Araxa, Brazil, pp. 115–128.

Montel, J.M., Foret, S., Veschambre, M., Nicollet, C., Provost, A., 1996. Electron microprobe dating of monazite. Chem. Geol. 131, 37–53.

Mosley, H.G.J., 1913. Philos. Mag. 26, 1024.

Mrose, M.E., Chao, E.C.T., Fahey, J.J., Milton, C., 1961. Norsethite, $BaMg(CO_3)_2$, a new mineral from the Green River Formation, Wyoming. Am. Mineral. 46, 420–429.

Myklebust, R.L., Newbury, D.E., 1994. Monte Carlo modeling of secondary X-ray fluorescence across phase boundaries in electron probe microanalysis. Scanning 17, 235–242.

O'Neill, HStC, 1980. An experimental study of Fe–Mg partitioning between garnet and olivine and its calibration as a geothermometer: corrections. Contrib. Mineral. Petrol. 72, 337.

O'Neill, HStC, Wall, V.J., 1987. The olivine–orthopyroxene–spinel oxygen geobarometer, the nickel precipitation curve, and the oxygen fugacity of the Earth's upper mantle. J. Petrol. 28, 1169–1191.

O'Neill, HStC, Wood, B.J., 1979. An experimental study of Fe–Mg partitioning between garnet and olivine and its calibration as a geothermometer. Contrib. Mineral. Petrol. 70, 59–70.

Packwood, R., 1991. A comprehensive theory of electron probe microanalysis. In: Heinrich, K.F.J., Newbury, D.E. (Eds.), Electron Probe Quantitation. Plenum, New York, pp. 83–104.

Peng, L., 1987. A study on inclusion in chromite of alpine-type ultrabasic rocks in western Jungar area of Xinjiang, China. Bull. Chin. Acad. Geol. Sci. 17, 103–118.

Peng, G., Lewis, J., Lipin, B., McGee, J., Bao, P., Wang, X., 1995. Inclusions of phlogopite and phlogopite hydrates in chromite from the Hongguleleng ophiolite in Xinjiang, northwest China. Am. Mineral. 80, 1307–1316.

Potts, P.J., 1987. A Handbook of Silicate Rock Analysis. Chapman and Hall, New York (622 pages).

Pouchou, J.L., Pichoir, F., 1986a. Basic expression of "PAP" computation for quantitative empa. In: Brown, J.D., Packwood, R.H. (Eds.), 11th Intl Congress on X-ray Optics and Microanalysis, p. 249.

Pouchou, J.L., Pichoir, F., 1986b. Very light elements X-ray microanalysis. Recent models of quantification. J. Microsc. Spectroscopie Electron. 11, 229–250.

Pouchou, J.L., Pichoir, F., 1988. A simplified version of the "PAP" model for matrix corrections in epma. In: Newbury, D.E. (Ed.), Microbeam Analysis, pp. 315–318.

Pouchou, J.L., Pichoir, F., 1991. Quantitative analysis of homogeneous or stratified microvolumes applying the model "PAP". In: Heinrich, K.F.J., Newbury, D.E. (Eds.), Electron Probe Quantitation. Plenum Press, pp. 31–75.

Reed, S.J.B., 1993. Electron Microprobe Analysis, 2nd ed. Cambridge University Press.

Reed, S.J.B., 1995. Electron microprobe microanalysis. In: Potts, P.J., Bowles, J.F.W., Reed, S.J.B., Cave, M.R. (Eds.), Microprobe Techniques in the Earth SciencesThe Mineralogical Society Series v 6. Chapman and Hall, pp. 49–90.

Reed, S.J.B., 2005. Electron Microprobe Analysis and Scanning Electron Microscopy in Geology, 2nd ed. Cambridge University Press, (189 pages).

Rovsha, V.S., 1962. On the composition of solid inclusions in diamond indicator minerals. Zap Vses Miner Obshch 91, pp. 603–605, (in Russian).

Smith, D.G.W., 1976. Short Course In Microbeam Techniques. Mineralogical Association of Canada, Edmonton (186 pages).

Steyn, J.G.D., Watson, M.D., 1967. Notes on a new occurrence of norsethite, $BaMg(CO_3)_2$. Am. Mineral. 52, 1770–1775.

Sundius, N., Blix, R., 1965. Norsethite from Långban. Ark. Mineral Geol. 4, 277–278.

Talkington, R.W., Lipin, B.R., 1985. Platinum-group-element-bearing inclusions in chromite of the ultramafic zone, Stillwater Complex, Montana; occurrence, chemistry and petrological significance. Can. Mineral. 23, 315–316.

Wang, L., Zhang, Y., Essene, E.J., 1999. Mineral inclusions in pyrope crystals from Garnet Ridge, Arizona, USA: implications for processes in the upper mantle. Contrib. Mineral. Petrol. 135, 164–178.

Wark, D.A., Watson, E.B., 2006. TitaniQ: a titanium-in-quartz geothermometer. Contrib. Mineral. Petrol. 152, 743–754.

Webb, S.A.C., Wood, B.J., 1986. Spinel–pyroxene–garnet relationships and their dependence on Cr/Al ratio. Contrib. Mineral. Petrol. 9, 471–480.

Williams, M.L., Jercinovic, M.J., Terry, M.P., 1999. Age mapping and dating of monazite on the electron microprobe: deconvoluting multistage tectonic histories. Geology 27, 1023–1026.

Zhang, Y., 1998. Mechanical and phase equilibria in inclusion–host systems. Earth Planet. Sci. Lett. 157, 209–222.

Zhao, D., 1998. Kimberlite, Diamond and Mantle Xenolith From Northwest Territories, Canada and North China(Ph.D. Thesis) University of Michigan, Ann Arbor, Michigan.

Zhao, D., 2012. Heterogeneity of the Kakanui hornblende standard at the University of Texas at Austin. Microanalytical Reference Materials Topical Conference Abstracts Volume. Microanalysis Society, Golden, Colorado.

Zhao, D., Essene, E.J., Zhang, Y., 1999. An oxygen barometer for rutile–ilmenite assemblages: oxidation state of metasomatic agents in the mantle. Earth Planet. Sci. Lett. 166, 127–137.

Ziebold, T.O., Ogilvie, R.E., 1964. An empirical method for electron microanalysis. Anal. Chem. 36, 322–327.